

High-temperature fluctuations of the deep ocean: an early Eocene clumped isotope (Δ_{47}) temperature record of ODP Site 1263, Walvis Ridge

GEO4-1520 MSc Thesis

B.L.P. (Bas) Koene

5620279

Utrecht University

Department of Earth Sciences

Final Version: 24-11-2021

Supervisors

Prof. Dr. Lucas J. Lourens

Dr. Martin Ziegler

Tobias Agterhuis, MSc

Abstract

The continued emissions of carbon-dioxide poses a threat to the global community, of which the magnitude depends on the sensitivity of the climate. However, constraints on the climate sensitivity are still very uncertain, and more pessimistic emission scenarios appear to become more relevant. Studying the climate of the early Eocene (56-47.8 Ma) hothouse presents us with a way to confine these uncertainties, and to investigate the mechanisms that may become relevant at higher carbon-dioxide levels.

In this study, deep ocean temperatures and seawater $\delta^{18}\text{O}$ are reconstructed using ‘clumped isotopes’ (Δ_{47}). As opposed to other temperature proxies, such as TEX_{86} , Mg/Ca and the classical $\delta^{18}\text{O}$, clumped isotopes are independent of seawater chemistry vital effects, and is purely thermodynamical. The clumped isotopes are measured on the *Nuttallides truempyi*, *Oridorsalis umbonatus*, *Cibicidoides* spp, and *Hanzawaia ammophila* benthic foraminifera species using isotope ratio mass spectrometry.

A total of six reconstructed temperatures spanning the entire early Eocene are presented. Of particular interest is the early Eocene Climate Optimum (EECO, ~51.5-49.5 Ma), a period in which Earth’s surface temperature culminated. A deep ocean warming of $\sim 7.22 \pm 4.44$ °C is recorded between 53 Ma and the EECO, after which a cooling of $\sim 5.29 \pm 4.37$ °C occurred in a few million years span, towards 48 Ma. These temperatures are not recorded by $\delta^{18}\text{O}$, and poorly in Mg/Ca, most likely due to problems with those proxies. A potential pH-effect in the $\delta^{18}\text{O}$ of benthic foraminifera is investigated, but the current understanding is insufficient for taking conclusions. Moreover, sea surface temperatures do not reflect changes in the deep ocean during the early Eocene, exposing problems with the calibrations for the TEX_{86} temperature proxy, as well as assumptions of surface and deep ocean coupling, usually done based on benthic $\delta^{18}\text{O}$ alone.

The $\delta^{18}\text{O}$ composition of the seawater ($\delta^{18}\text{O}_w$) has been recalculated for the Eocene, revealing much heavier values than conventionally assumed. $\delta^{18}\text{O}_w$ values as heavy as 0.61 ‰ VSMOW were recorded, which was usually taken to be -0.98 ‰, assuming that the early Eocene was ice-free. This puts forward a series of complications that need explaining with regard to the origin of the $\delta^{18}\text{O}_w$ and overall ocean circulation, which are explored here.

New estimates for climate sensitivity during the EECO reveal a temperature change of 6.0 °C per doubling in carbon-dioxide (CO_2), with a maximum of 9.1 °C minimum of 4.1 °C. This is higher than estimates based on benthic $\delta^{18}\text{O}$. The new Δ_{47} -derived climate sensitivity is in line with a recent climate model simulation which contains enhanced cloud microphysics, and agrees with a recent Mg/Ca temperatures and boron-based CO_2 study. The findings here support a climate-state dependency of climate sensitivity.

Altogether, clumped isotope thermometry brings the need for critically re-evaluating long-standing assumptions, which may in the end help in a better understanding of the Earth System, and thus establishing better climate models and predictions for future climate warming.

Table of contents

Abstract.....	2
Table of contents	3
1. Introduction	4
1.1 Early Eocene climate.....	4
1.2 Clumped isotope thermometry.....	5
1.3 Research aims	7
2. Materials and methods.....	8
2.1 Site descriptions and sampling	8
2.2 Sample preparation and micropaleontology.....	9
2.3 Clumped isotope thermometry.....	12
2.3.1 Instrumental setup.....	12
2.3.2 Complications and corrections.....	13
2.3.4 Temperature and $\delta^{18}\text{O}_w$ calculations.....	14
2.3.5 Analytical uncertainties and error propagation.....	15
3. Results	16
4. Discussion.....	18
4.1. Deep ocean temperatures as derived from Δ_{47} , $\delta^{18}\text{O}$, and Mg/Ca.....	18
4.2 The $\delta^{18}\text{O}_w$ composition of deep waters	20
4.3 The pH effect of $\delta^{18}\text{O}_b$ and Δ_{47}	22
4.4 Sea surface – deep ocean mismatch.....	22
4.5 Circulation and water masses	24
4.6 Global mean surface temperature and climate sensitivity	25
5. Conclusions	27
Acknowledgements	28
Appendix: Foraminifera glossary.....	29
References.....	30

1. Introduction

1.1 Early Eocene climate

The Earth's climate is undergoing major changes under the influence of anthropogenic carbon emissions, of which the effects are observed in the oceans, atmosphere, cryosphere, and biosphere (IPCC 2014). The consequence of this global change presents the global population with challenges that highly depend on the severity of the magnitude of these changes. As of yet, the magnitudes of changes in each of these spheres are highly uncertain. One of the most important questions is that of climate sensitivity, the change of global mean surface temperature with every doubling of CO_2 (IPCC 2014). The current anthropogenic emission of carbon may, under the worst case scenario of RCP 8.5, lead to CO_2 levels close to that of the Eocene (56–33.9 Ma), which is known as a 'Hothouse' (Zachos, Dickens, and Zeebe 2008). Therefore, studying the climate of the Eocene may give answers to the states and transitions which lie ahead in the coming century.

The beginning of the Eocene (Ypresian) is marked by the Paleocene-Eocene Thermal Maximum (PETM, ~56 Ma), the first of a series of transient warming events throughout the Eocene known as 'hyperthermals' (Lourens et al. 2005; Zachos, Dickens, and Zeebe 2008; Sluijs et al. 2007; Bowen et al. 2014). It is associated with the rapid release of carbon from the deep oceans, for which several hypotheses exist, including astronomical forcing, oceanic circulation changes, volcanism, and others (Zachos et al. 2005; Kent et al. 2003; Jones et al. 2019; Lourens et al. 2005). Following the PETM, the Early Eocene climate warmed and culminated at the early Eocene Climate optimum (EECO), punctuated still by hyperthermal events (Figure 1.1, Lourens et al. 2005; Zachos, Dickens, and Zeebe 2008; Sluijs et al. 2007; Bowen et al. 2014; Lauretano et al. 2015). The PETM and early Eocene hyperthermals are paced by the long (405 kyr) and short (100 kyr) eccentricity cycles (Lourens et al. 2005; Lauretano, Zachos, and Lourens 2018). Global mean surface temperatures (GMSTs) of the EECO are estimated to span 22.2–30.7 °C (90% CI), on average 13 °C warmer than at present day (Inglis et al. 2020).

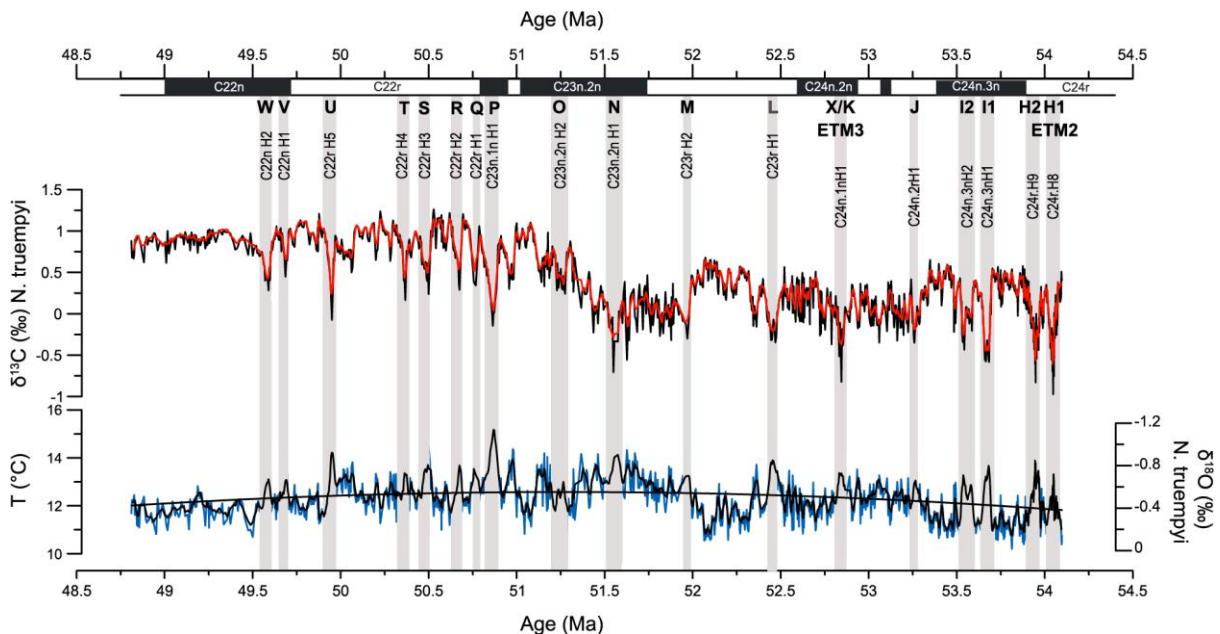


Figure 1.1: Early Eocene record with superimposed hyperthermals. Adapted and modified from Lauretano, Zachos, and Lourens (2018).

A feature of particular interest within the EECO is the enigmatic early Eocene Carbon Shift (EECS). It occurs between ~51.6 and ~51.0 Ma at Site 1263 and between ~51.2 and 51.0 Ma at Site 1209 (Lauretano et al. 2016; Lauretano, Zachos, and Lourens 2018; Westerhold et al. 2018). The +0.75 ‰ shift in $\delta^{13}\text{C}$ could be the result of a critical transition as indicated by the unstable record preceding it (Westerhold et al. 2018; Lauretano, Zachos, and Lourens 2018). This could be due to a reorganisation in the plate-mantle system, changes in seafloor-spreading, and chaotic diffusion of planetary orbits in the solar system (Westerhold et al. 2018), although these causes remain speculative (Lauretano, Zachos, and Lourens 2018).

1.2 Clumped isotope thermometry

Traditionally, marine temperatures are inferred from oxygen stable isotopes as the thermodynamic properties of isotopes depend on their atomic mass (Urey 1947). Following this relationship, the temperature of the formation of carbonate can be determined by measuring the isotope ratios (Epstein et al. 1951). Ever since, other chemical proxies such as carbonate Mg/Ca, TEX_{86} , or U^{K}_{37} have also been utilized to determine temperatures. However, such proxies, including oxygen isotopes, are prone to error due to their dependency on a multitude of external factors other than temperature alone. For one, stable oxygen isotope ratios ($\delta^{18}\text{O}$) have a dependency on the stable isotopic composition of the source water of the foraminifers environment, as well as biotic effects of the foraminifer itself (Ravelo and Hillaire-Marcel 2007). Another temperature proxy using foraminifera is Mg/Ca, which is subject to changes in the concentration of either Mg or Ca elements, of which ratios vary through geologic time (Evans and Müller 2012). Organic proxies such as TEX_{86} or U^{K}_{37} depend on different species effects (Conte et al. 1995), selective degradation (Huguet et al. 2009), and transportation processes (Mollenhauer et al. 2005), and are limited to the upper layers of the ocean, where the biomarker-producing organisms reside. Additionally, the sensitivity in calibrations for TEX_{86} are uncertain because the production depths of the used tetra-ether lipids are unclear (Shah et al. 2008; Hollis et al. 2012; Zhang, Pagani, and Wang 2016), and other effects than temperature may be of influence (Tierney 2013).

Multiply-substituted isotopologues, or ‘clumped isotopes’, are a novel proxy for studying past temperatures. Clumped isotopes are molecules in which two or more conventional isotopes are substituted with heavier, rare isotopes (Eiler 2007). The fractionation of such clumped isotopes is purely thermodynamical, negating external effects such as water composition (Wang, Schauble, and Eiler 2004; Tripathi et al. 2010).

Following the ‘rule of the geometric mean’, it is assumed that the substitution of two heavy isotopes over two regular isotopes has exactly twice the change in bond energy (Bigeleisen 1955; Eiler 2007). This would mean that there is no preference for clumping and that a fully stochastic distribution follows, such that there is no enthalpy of mixing (Eiler 2007; Bigeleisen 1955). However, this is only true for high temperatures, and in practice there is a preference for bonding of heavy isotopes at lower temperatures (Eiler 2007). Depending on the clumped isotope species, there is a different degree of deviation from the fully random (stochastic) distribution (see Figure 1.2), notated as ‘ Δ ’ (Wang, Schauble, and Eiler 2004; Ghosh et al. 2006). Generally, the heavier the isotopologues, the stronger the temperature dependence.

Unfortunately, the heaviest isotopologues are also the rarest, making high-precision measurements difficult (Ghosh et al. 2006). For thermometry, the most applied clumped isotope is Δ_{47} , which is in practice the deviance of $^{13}\text{C}^{18}\text{O}^{16}\text{O}$ from the stochastic. It has a moderately strong temperature dependence, and is the commonest occurring clumped isotope (Eiler 2007; Ghosh et al. 2006).

The Δ_{47} values can be calculated according to Equation 1.1 (Eiler 2007):

$$(1.1) \quad \Delta_{47} = \left[\left(\frac{R_{47}}{R_{47}^*} - 1 \right) - \left(\frac{R_{46}}{R_{46}^*} - 1 \right) - \left(\frac{R_{45}}{R_{45}^*} - 1 \right) \right] \times 1000$$

Where:

- R_i is the measured ratio of the masses 47, 46, and 45 over mass 44;
- R_i^* is the ratio of the masses 47, 46, and 45 over mass 44 following a stochastic abundance.

The pure, thermodynamic dependency of clumped isotopes gives a threefold of advantages over regular isotope ratio mass spectrometry: (1), the temperature of formation can be derived directly from a single phase without correction for external factors, and following this, (2), the water composition and biotic components can then be extracted from the $\delta^{18}\text{O}$ values, and (3) the regular $\delta^{18}\text{O}$ and $\delta^{13}\text{C}$ are obtained in the same measurement. In recent times, mass spectrometry has advanced sufficiently to provide the precision required for measuring these clumped isotope ratios reliably (Eiler and Schauble 2004).

The primary limiting factor, however, is instrumental precision, because all clumped isotopes species together constitute only 100 ppm abundance in nature (Ghosh et al. 2006). A high number of replicate measurements are required to resolve this low analytical precision (Huntington et al. 2009). High-precision measurements previously required 15 mg of sample using the conventional Dual Inlet (DI) system. The more recent Long Integration Dual Inlet (LIDI) workflow now allows samples 40 times

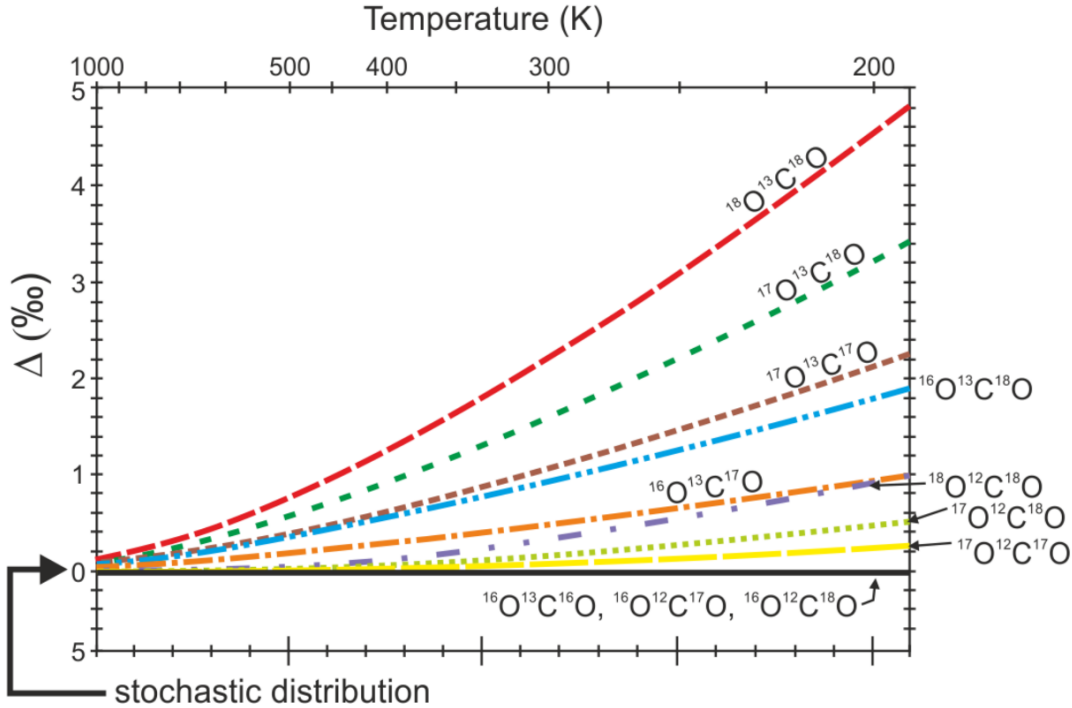


Figure 1.2: The deviation from the stochastic distribution of several carbon-dioxide species. Modified and adapted after Wang, Schauble, and Eiler (2004).

smaller ($\sim 100 \mu\text{g}$), by utilizing a more efficient way to integrate the sample gas, resulting in less sample gas waste (Müller et al. 2017). This allows the measurement of the scarce Eocene foraminifera of ODP samples.

Other uncertainties arise from the same complications as regular stable isotopes, such as recrystallization or diagenesis (Leutert et al. 2019), and a potential pH effect, although the effect of the latter is considered minimal for Δ_{47} by recent experiments (Tripathi et al. 2015; Guo 2020). Lastly, there is a divergence between laboratories in calibrations and methodologies (Hollis et al. 2019 and references therein). Fortunately, a growing amount of effort is put in the development of methodologies and standardization to reduce uncertainties further (Meckler et al. 2014; Bernasconi et al. 2018).

Temperatures from clumped isotopes, like Mg/Ca, allow calculation of $\delta^{18}\text{O}_w$ for the past oceans, although in contrast to Mg/Ca, without the caveats of nonthermal effects (Leutert et al. 2020). Clumped isotope analysis has revealed that the assumption of -0.98‰ for $\delta^{18}\text{O}_w$ of the Eocene oceans may be incorrect, and in fact varies over the Early Eocene (Meckler et al., *in pre-print*). This assumption was based on the non-existence of major ice sheets in the Early Eocene, which leaves all the highly negative ice sheet $\delta^{18}\text{O}$ (^{16}O -rich) waters to the open oceans (Zachos et al. 2001; Cramer et al. 2011). The deviance of $\delta^{18}\text{O}_w$ is as of yet not explained and requires further research.

1.3 Research aims

Here, I aim to study deep-sea benthic foraminifera from Ocean Drilling Program (ODP) Site 1263 to get better estimates of the deep water temperatures during the Early Eocene. Doing so enables the assessment of Δ_{47} -temperatures in comparison with other temperature proxies, and providing better understanding of past ocean water compositions. In turn, this may help to shed light on future climates and climate sensitivity. Climate sensitivity remains a key question as to what extent carbon-dioxide emissions will have to be limited, or even captured.

Deep water temperatures allow the investigation of past climates with much more certainty and reliability than surface waters, as the deep ocean is insulated and responds in a sluggish fashion to change, protecting it from seasonal and geographical perturbations (Lear, Elderfield, and Wilson 2000). Additionally, benthic foraminifera are usually much better preserved than planktic foraminifera (Schrag, DePaolo, and Richter 1995; Edgar, Pälike, and Wilson 2013), which would otherwise lead to inaccuracies in the measurement of stable isotopes.

2. Materials and methods

2.1 Site descriptions and sampling

Walvis Ridge is an aseismic ridge dividing the eastern South Atlantic into the Angola Basin in the north, and the Cape Basin in the south (Shipboard Scientific Party 2004). It was drilled for a second time during ODP Leg 208 to complement the original expedition to the area, DSDP Leg 74, which suffered incomplete core recovery and disturbances. ODP Leg 208 includes 6 sites at various water depths, of which the shallowest, Site 1263, will be studied here (see Figure 2.1 for an overview of the depths and the locations of Leg 208).

Site 1263 ($28^{\circ}31.98'S$, $02^{\circ}46.77'E$) is situated at a water depth of 2712 m and spans the Cenozoic until the upper Paleogene, and it has lied above the CCD throughout the Cenozoic (Shipboard Scientific Party 2004). Its stratigraphy is constant, consisting of mostly calcareous nannofossil oozes and chalk. It is divided into one lithostratigraphic unit and three subunits. Subunit IA (0-99.1 mcd) consists of a

foraminifer-bearing nannofossil ooze and regular nannofossil ooze, spanning the upper Eocene to Pleistocene; subunit IB (99.1-318 mcd) consists of a regular, a clay-bearing, and chalky nannofossil

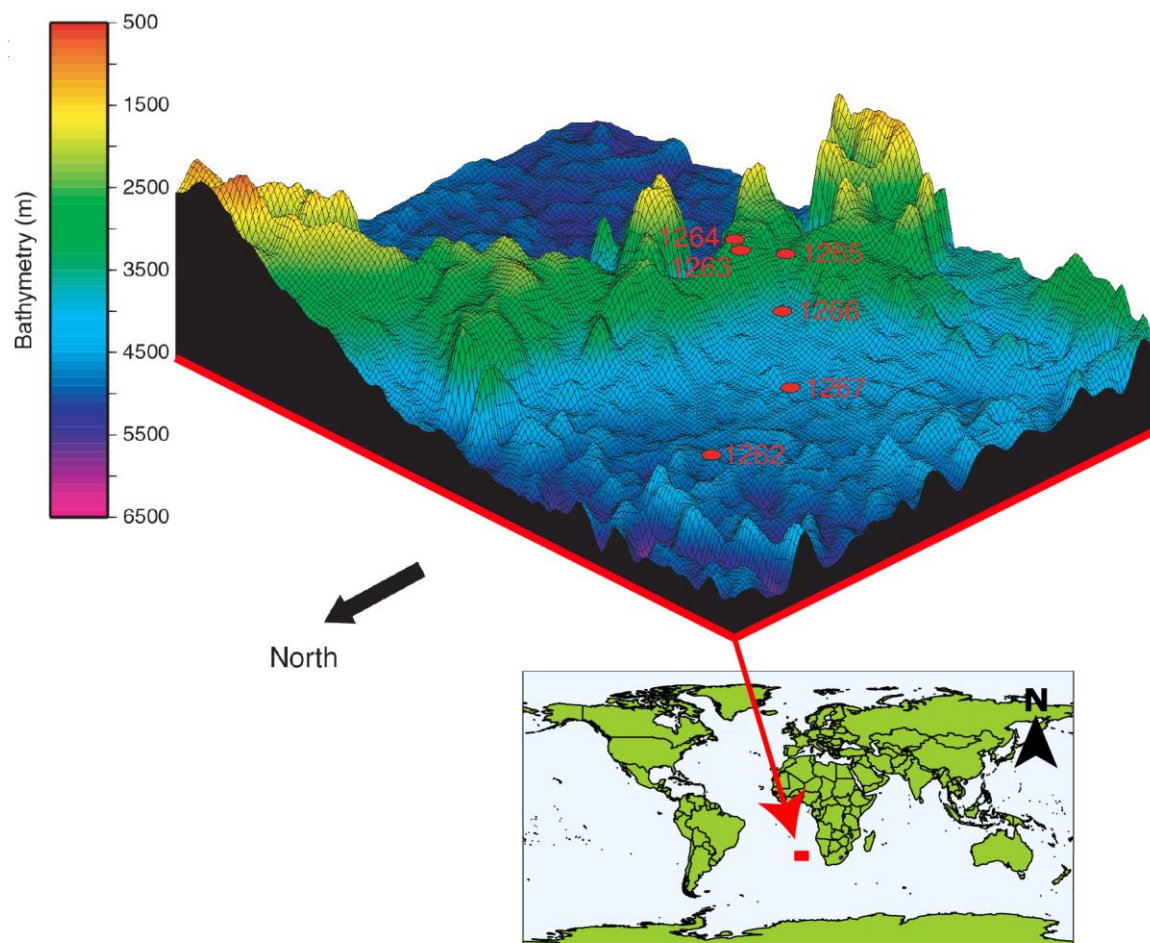


Figure 2.1: Bathymetric map of Leg 208 sites and their locations on the world map. Modified after Shipboard Scientific Party (2004).

oozes, spanning only parts of the Eocene; subunit IC (318-400.7 mcd) contains a regular and a chalky nannofossil ooze spanning the upper Paleocene until the lowermost Eocene.

The age model of Site 1263 has been established by means of magnetostratigraphy, biostratigraphy, and astronomically tuned stable isotopes and x-ray fluorescence data (Lauretano et al. 2015, 2016; Westerhold et al. 2017; Lauretano, Zachos, and Lourens 2018). Samples were taken every 1 cm where available for the studied core sections.

A few intervals were chosen for Site 1263 to complement the record by Meckler et al. (*in pre-print*). For Site 1263, core sections that roughly correspond to the interval between the X/K and J events (53.25-52.90 Ma) were selected, as well as an arbitrary interval in the wake of the EECO (48.19-48.08 Ma). Given the previous extensive sampling on the original splice of both sites, the sampling of this study has been done on alternative holes, which was checked by correlating magnetic susceptibility and using the splice tie points for Site 1263 by Westerhold et al. (2017) and Lauretano, Zachos, and Lourens (2018).

2.2 Sample preparation and micropaleontology

All samples were freeze-dried and then washed with warm tap water through three sieves, resulting in >150, >63, and >38 μm fractions. The material was retrieved from the sieves using DI water, transferred to glass bowls, after which the fractions were left to dry overnight in an oven at 40 °C. The dry samples of the three fractions were then conveyed to glass pots.

The samples were picked for the *Nuttallides truempyi* and *Oridorsalis umbonatus* benthic foraminifera species to allow direct comparison with other Eocene clumped records. Their morphologies are shown in Figure 2.2. Foraminifera photographs were obtained using a Keyence VHX-5000 series digital microscope. The species definitions of Holbourn, Henderson, and MacLeod (2013) were used, extended with the observed characteristics of the foraminifera in the studied core sections. A foraminifera glossary with the definitions of the foraminifera characteristics as used here can be found in the Appendix.

Nuttallides truempyi forms a test with a lobulate outline, of which the cross-section appears planoconvex to biconvex, with an acute and imperforate keeled periphery. The chambers are divided in a crescentic shape, which increase slowly in size throughout the whorl. It is evolute on the spiral side. The chamber walls are smooth and finely perforate. The umbilical side displays a clear, imperforate umbilical boss. The aperture is an interiomarginal slit which reaches from the umbilical boss to nearby the periphery. Their diameter was typically 250 μm for core section 1263B 16H1W and 220 μm for core sections 1263B 23H3W and 23H4W.

Oridorsalis umbonatus forms tests subcircular to lobulate in outline, and biconvex in cross-section. The chamber sutures are slightly crescentic on the spiral side, and straight on the umbilical side. The chamber walls are finely perforate and smooth. The aperture is an interiomarginal slit, strongly exposed to the umbilical side when looked at in cross-section and extends well out towards the periphery. Their diameter was typically 230 μm for core section 1263B 16H1W, and 220 μm for 1263B 23H3W and 23H4W.

Both *Nuttallides* and *Oridorsalis* were fairly limited in the studied core sections. Therefore, they have been supplemented with *Cibicidoides* spp. and *Hanzawaia ammophila* where available. *Cibicidoides* spp. consisted of *Cibicidoides eoceanus* and the *Cibicidoides mundulus* group (E. Thomas, personal communication, September 2021).

Cibicidoides eoceanus is trochospiral, and often strongly planoconvex in cross-section. The chambers gradually increase in size over the final whorl, with clear separation on the umbilical side. The test walls are coarsely perforate, especially on the spiral side. A prominent umbilicus is present. The

aperture is a narrow slit that extends unto the spiral side and displays a thin lip. Specimen could be very large, reaching sizes of over 300 µm in 1263B 16H1W.

The *Cibicidoides mundulus* group is interpreted as *Cibicidoides praemundulus*, although a specific designation could not be given. Nonetheless, its characteristics are used here. It forms a biumbonate trochospire, mostly biconvex in cross-section. Similarly to *Cibicidoides eocaenus*, its chambers gradually increase, and it can be coarsely perforate on the spiral side, although it usually appears more glossy. Its aperture is also highly similar. Specimen were usually much smaller than that of *Cibicidoides eocaenus*.

Hanzawaia ammophila (synonymous with *Hanzawaia cushmani*, Holbourn, Henderson, and MacLeod 2013) displays a small trochospire and is planoconvex in cross-section. It has an imperforate periphery with subrounded outline. The chambers increase rapidly in size in the last whorl, and are strongly separated by thin and curved sutures that are depressed at the umbilical side and raised at the spiral side. The chamber walls are finely perforate and smooth on both sides. Its primary aperture was difficult to distinguish, but forms a narrow slit that extends to the spiral side. Specimen varied in size and occurrence over the core sections. It was typically ~250 µm and rare in 1263B 23H3W and 23H4W, whereas it could reach sizes of 300 µm and appeared more commonly in 1263B 16H1W.

After picking, the foraminifera were crushed between glass slides and transferred to Eppendorf tubes (0.5 mL) using DI water. The excess water was removed. Subsequently, the tubes were put in an ultrasonic bath and exposed for approximately 30 seconds. After the ultrasonic treatment, the waste materials (organics, nannofossils) were brought in suspension by tapping the tubes, and the suspension removed by pipetting. The ultrasonic treatment was repeated until the water was clean of waste material, after which the Eppendorf tubes were left to dry overnight at room temperature under a plastic cover.

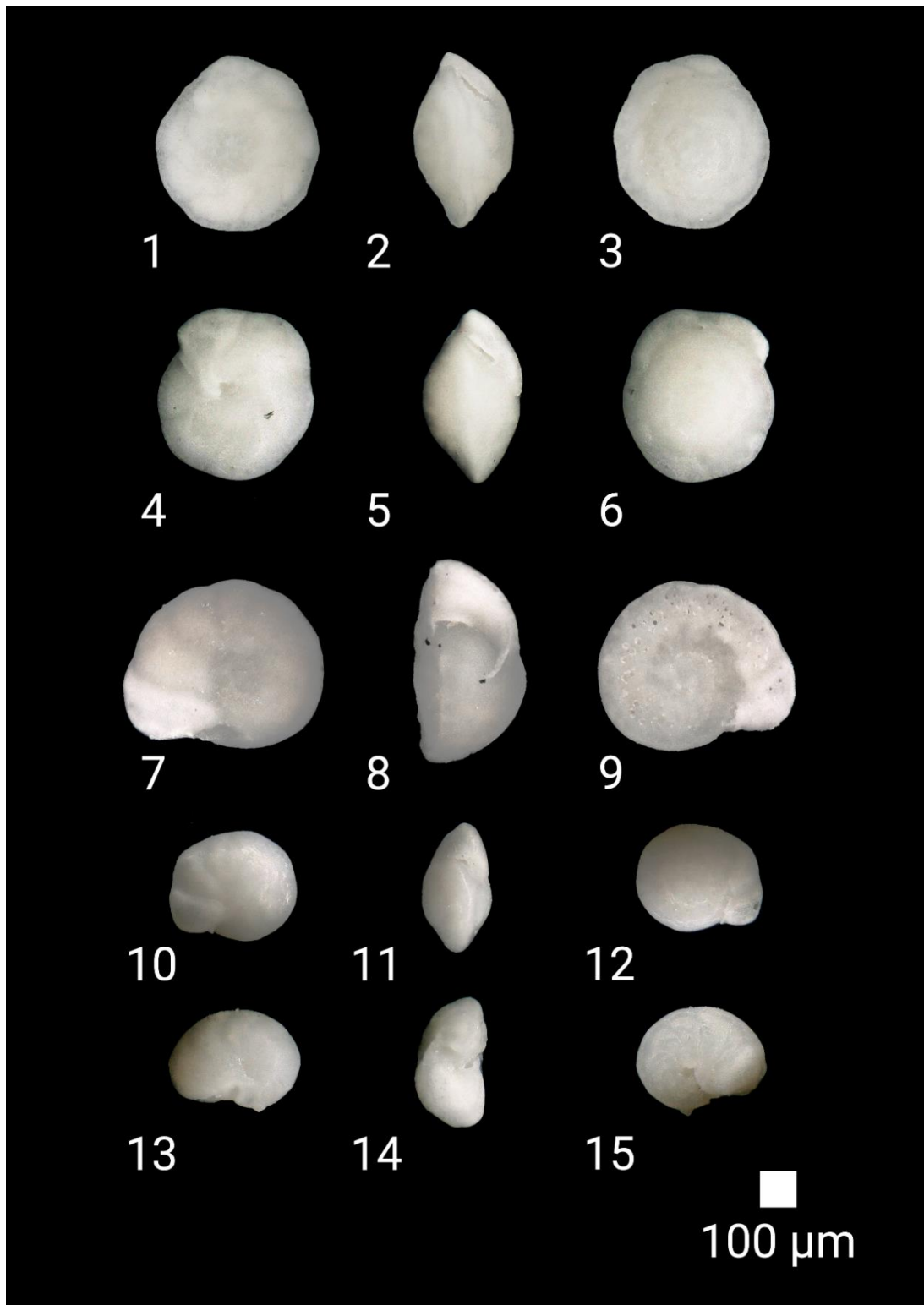


Figure 2.2: Foraminifera plates: (1) *Nuttallides truempyi* umbilical view, (2) apertural view, (3) spiral view (1263B 16H1W 84-85 cm); (4) *Oridorsalis umbonatus* umbilical view, (5) apertural view, (6) spiral view (1263B 16H1W 21-22 cm); (7) *Cibicidoides eocaenus* umbilical view, (8) apertural view, (9) spiral view (1263B 23H4W 54-55 cm); (10) *Cibicidoides mundulus* group umbilical view, (11) apertural view, (12) spiral view (1263B 23H4W 12-13 cm); (13) *Hanzawaia ammophila* umbilical view, (14) apertural view, (15) spiral view (1263B 23H4W 12-13 cm). Note that the exposure curves for the photos have been adjusted for better clarity.

2.3 Clumped isotope thermometry

2.3.1 Instrumental setup

Stable isotope ratio mass spectrometry measurements were performed at the Utrecht University GeoLab, using the stable isotope facilities during a period of three weeks from September 13th to October 1st, 2021. The measurements were done using a *Thermo Scientific Kiel IV Carbonate Device* coupled to a *Thermo Scientific 253 Plus 10 kV* isotope ratio mass spectrometer. Between 70-90 μg of samples and ETH-1, ETH-2, ETH-3, MERCK, and IAEA-C2 standards were weighed in. The used accepted values for the standards are given in Table 2.1. One run consisted of 46 measurements, of which 22 samples, and 24 standards, in accordance with Kocken, Müller, and Ziegler (2019). The workflow was as follows (see Figure 2.3): The samples and standards in their vials were loaded in the carousel of the *Kiel IV*. The samples and standards were dissolved in a vacuum at 70 °C using 102-105 % phosphoric acid. The resulting CO_2 gas was trapped in a first liquid nitrogen trap at -196 °C. The trap was heated to 100 °C to allow movement of the CO_2 through a *Porapak-Q* Mesh trap at -50 °C, which filters halo-, hydrocarbons and sulphides (Müller et al. 2017). Afterwards, the CO_2 gas was captured in a last liquid nitrogen trap at -196 °C. Finally, micro-volume mode was used to transfer the CO_2 gas into the mass spectrometer for measurement. The *Thermo Scientific 253 Plus* was equipped with Faraday cups for $m/z = 44, 45, 46, 47$,

Table 2.1: Accepted values for used standards.

Standard	$\delta^{13}\text{C}$ (‰ VPDB)	$\delta^{18}\text{O}$ (‰ VPDB)	Δ_{47} (I-CDES90°C)
Reference gas	-4.670	-2.820	
ETH-1	$2.02 \pm 0.03^*$	$-2.19 \pm 0.04^*$	$0.2052 \pm 0.0016^\dagger$
ETH-2	$-10.17 \pm 0.06^*$	$-18.69 \pm 0.11^*$	$0.2085 \pm 0.0015^\dagger$
ETH-3	$1.71 \pm 0.02^*$	$-1.78 \pm 0.06^*$	$0.6132 \pm 0.0014^\dagger$
IAEA-C2	$-8.25 \pm 0.02^*$	$-8.94 \pm 0.04^*$	$0.6445 \pm 0.0021^\dagger$
MERCK	$-41.91 \pm 0.02^\ddagger$	$-15.62 \pm 0.01^\ddagger$	$0.5151 \pm 0.0034^\dagger$

*Bernasconi et al. (2018), table 4; † Bernasconi et al. (2021), table 1; ‡ Müller et al. (2019), table 4. Uncertainties are reported as 1SE.

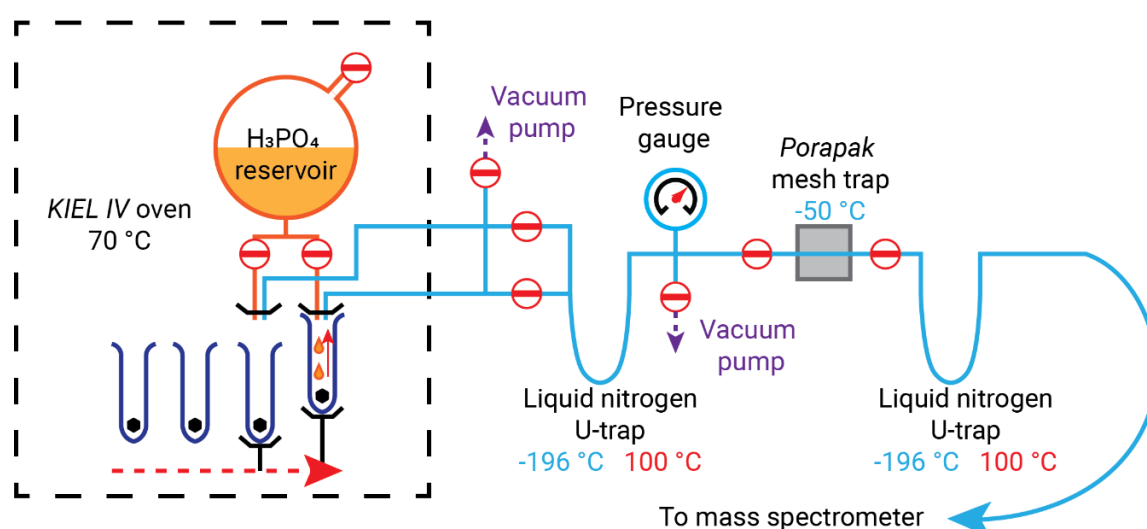


Figure 2.3: Schematic of the KIEL IV Carbonate Device. Modified after Spencer and Kim (2015).

47.5, 48, and 49, of which cup 47.5 is meant for monitoring the background over mass 47. The Long Integration Dual Inlet (LIDI) workflow (*sensu* Müller et al. 2017) was used for all measurements. Using the LIDI workflow, the Dual Inlet will first measure all sample gas before going through with the reference gas, such that as little gas as possible is wasted.

2.3.2 Complications and corrections

A few complications may arise during the measurement of clumped isotopes. Firstly, isotope exchange may occur with the stainless-steel capillary of the mass spectrometer (Passey et al. 2010). This could be resolved by replacing the stainless-steel capillaries with Electroformed Nickel (EFNi) capillaries, minimizing isotopic exchange (Spencer and Kim 2015; Passey et al. 2010), although reportedly the stainless-steel capillaries at Utrecht University are not affected (Ziegler, M., personal communication, June 2021).

Secondly, recombination of CO₂ isotopologues at the ion source pushes the analyte towards a stochastic distribution (Huntington et al. 2009). This can be addressed by lowering the CO₂-pressure and residence time of the gas in the ion source (Huntington et al. 2009).

Thirdly, the ion beam for mass 44 has an electron scattering effect, as the top of the ion beam collides with the flight tube (He, Olack, and Colman 2012). The resulting secondary electrons are detected by the Faraday collectors, which measure a more negative voltage due to the negative electron charge, lowering the final signal for that collector. The scattering effect is strengthened linearly with higher partial CO₂-pressure, hence it is deemed the ‘pressure baseline effect’ (He, Olack, and Colman 2012; Bernasconi et al. 2013; Meckler et al. 2014). Although the effect is only a few mV, it is significant for Δ_{47} , as the total signal is typically only 2.5 V (He, Olack, and Colman 2012). Moreover, broadening of the mass 44 ion beam by coulombic repulsion causes some ⁴⁴(CO₂)-ions to be collected by the more sensitive Faraday collectors ($m/z = 47, 48, 49$), which causes an asymmetry in the baseline (He, Olack, and Colman 2012). The pressure baseline effect can be resolved by measuring the reference gas at different acceleration voltages (between 9.4-9.6 kV) as well as collector signal voltages (25, 20, 15, 10, and 5 V) resulting in peak scans. The backgrounds were then removed using simple linear regressions and interpolation (Meckler et al. 2014). Corrections for the pressure baseline effect were conducted in accordance with the methodology outlined by Meckler et al. (2014).

After correcting for the pressure baseline, the bulk composition (δ_{47}) and the total clumping (Δ_{47}) of the standards was checked. The three standards (ETH-1, ETH-2, and ETH-3) were chosen for corrections. ETH-1 is a heated carbonate with a low Δ_{47} and a high δ_{47} ; ETH-2 is heated to the same temperature, although has a different bulk composition (δ_{47}); ETH-3 has a δ_{47} similar to ETH-1, but has been precipitated at a much lower temperature, and thus a higher Δ_{47} . Plotting the measured and the accepted values for the Δ_{47} of these standards allow the construction of an empirical transfer function (ETF, Equation 2.1) that converts the measured Δ_{47} -values of samples onto the I-CDES90°C (InterCarb carbon-dioxide equilibrium scale) absolute reference frame, enabling inter-laboratory comparison (Dennis et al. 2011; Bernasconi et al. 2018, 2021).

$$(2.1) \quad \Delta_{47} \text{ (I-CDES90°C)} = a \times \Delta_{47 \text{ raw}} + b$$

- Where a is the slope of the regression and b its intercept;
- $\Delta_{47 \text{ raw}}$ are the measured values;
- $\Delta_{47} \text{ (I-CDES90°C)}$ are the values within the I-CDES90°C absolute reference frame (Bernasconi et al. 2021).

To avoid contaminations, the *Porapak-Q* mesh trap was heated to 150 °C for at least 1.5 hrs after every run with the vacuum lines opened on both sides of the trap. Any contaminations were closely monitored using the so-called '49 parameter', defined in Equation 2.2 (John and Bowen 2016).

$$(2.2) \quad 49 \text{ parameter} = [R_{\text{sample}}^{49} - R_{\text{working gas}}^{49}] \times 10^4$$

- Where R^{49} is the ratio of the measurement intensity of mass 49 over that of mass 44.

Any measurements with a 49 parameter over 0.200 and/or an internal Δ_{47} standard deviation of over 0.150 were labelled as outliers and were not used.

2.3.4 Temperature and $\delta^{18}\text{O}_w$ calculations

The temperature calibration by Meinicke et al. (2020), modified by Meinicke et al. (2021) for the I-CDES90°C reference frame of Bernasconi et al. (2021), was used to convert the corrected, absolute reference frame data into a temperature of formation (Equation 2.3).

$$(2.3) \quad \Delta_{47} (\text{I-CDES90}^\circ\text{C}) = (0.0397 \pm 0.0011) \times \frac{10^6}{T^2} + (0.154 \pm 0.0128)$$

- Where T is the final temperature in Kelvin.

Following the calculation of the calcite temperature of formation, it is now possible to extract the temperature effect from the $\delta^{18}\text{O}$, resulting in the $\delta^{18}\text{O}_w$ of the deep ocean seawater. Moreover, the I-CDES90°C reference frame ETH standard corrections are only applied to Δ_{47} , so additional corrections for acid fractionation must be carried for the final $\delta^{18}\text{O}$ and $\delta^{13}\text{C}$. The correction is calculated with Equation 2.4, using an acid fractionation correction factor ($\alpha\text{-CO}_2$) of 1.00871 (Kim, Mucci, and Taylor 2007).

$$(2.4) \quad \delta^{18}\text{O}_{\text{VPDB-CO}_3^{2-}} = \frac{(\delta^{18}\text{O}_{\text{VPDB-CO}_2} + 1000)}{(1.00871 - 1000)}$$

In order to use the oxygen isotope temperature calibration for *Cibicidoides* spp. of Marchitto et al. (2014), the measured stable isotopes have to be corrected for interspecies vital effects. The modifications according to Katz et al. (2003) are included in Table 2.2.

Finally, the oxygen isotope temperature calibration of Marchitto et al. (2014) was used to calculate the final $\delta^{18}\text{O}_w$ (equation 2.5).

$$(2.5) \quad \delta^{18}\text{O}_{\text{CaCO}_3(\text{VPDB})} - \delta^{18}\text{O}_{w(\text{SMOW})} + 0.27 = -0.245t + 0.0011t^2 + 3.58$$

- Where t is the temperature in degrees Celsius.

Table 2.2: interspecies calculations (Katz et al. 2003).

Species	Isotope	Correction factor*
<i>N. truempyi</i>	$\delta^{18}\text{O}$	(Nutt + 0.10)/0.89 = Cib
<i>N. truempyi</i>	$\delta^{13}\text{C}$	Nutt + 0.34 = Cib
<i>Oridorsalis</i> spp.	$\delta^{18}\text{O}$	Orid - 0.28 = Cib
<i>Oridorsalis</i> spp.	$\delta^{13}\text{C}$	Orid + 0.72 = Cib
<i>Hanzawaia ammophila</i>	$\delta^{18}\text{O}$	(Hanz - 0.16)/0.62 = Cib
<i>Hanzawaia ammophila</i>	$\delta^{13}\text{C}$	Hanz + 0.08 = Cib

*Cib = *Cibicidoides* spp.; Nutt = *Nuttallides truempyi*; Orid = *Oridorsalis* spp.; Hanz = *Hanzawaia ammophila*.

2.3.5 Analytical uncertainties and error propagation

A threefold of errors can be distinguished that are included in the final Δ_{47} -temperatures: (1) the measurement error as a result of analytical uncertainty, lab handling and other external influences, (2) the uncertainty of the ETF, and (3) the uncertainty of the temperature calibration that is utilized.

Most of the error introduced by the instrumentation (1) is compensated for by the PBL-corrections. Errors introduced by the ETF calculations (2) can mostly be resolved by using the recommendations as addressed by Kocken, Müller, and Ziegler (2019). These include using a minimal samples-to-standards ratio of 1:1 within every individual run, using standards that are close in Δ_{47} to the sample values. Therefore, measurements performed here adhere to those recommendations, and further extensive ETF-uncertainty calculations have been ignored as they are beyond the scope of this study. The long-term reproducibility of the instrument is monitored using IAEA-C2 and MERCK international standards.

Calibration uncertainties and measurement error were addressed by applying error propagation. The Meinicke et al. (2020) calibration was propagated using a *Matlab* script that utilized a variance-covariance matrix of the slopes and intercepts, following the mathematics of the supplement of Huntington et al. (2009). It should be noted that the calibration error is very small compared to the analytical error, with a maximum of 0.11 °C share of the total error in this study.

3. Results

A total of five bins were produced, consisting of 48 Ma (47.9-48.1 Ma), the EECO (50.8-51.2 Ma), 51.5 Ma (51.5-52 Ma), 52 Ma (52.1-52.3 Ma), and 53 Ma (53.0-53.1 Ma). A sixth bin composed of the ETM-2 is also included here (53.9-54.1 Ma), but is taken from Agterhuis, et al. (*in pre-print*). Of all bins, the temporal ranges were taken such that ‘background’ conditions were measured, negating hyperthermals. For ETM-2, this meant including only the measurements with a $\delta^{18}\text{O}$ of -1.5‰ and heavier, corresponding to the ‘background’ as mentioned in Agterhuis, et al. (*in pre-print*).

The results of each of the bins are shown in a time series in Figure 3.1, using the age model of Westerhold et al. (2017). Ages have been converted directly from sample depth (mbsf). The bins of the EECO, 51.5 Ma, 52 Ma, and the ETM-2 consist of measurements on either *Nuttallides truempyi* or *Oridorsalis umbonatus*. The 48 Ma and 53 Ma bins were scarce in benthic foraminifera, and thus *Cibicidoides* spp. and *Hanzawaia ammobhila* had to be utilized as well. This should not make a difference for Δ_{47} , given their ecology is similar, although additional species-specific corrections as described in paragraph 2.2 had to be performed for both $\delta^{18}\text{O}$ and $\delta^{13}\text{C}$.

The average benthic Δ_{47} values were 0.632 ± 0.010 for 48 Ma, 0.615 ± 0.009 for the EECO (51 Ma), 0.623 ± 0.007 for 51.5 Ma, 0.629 ± 0.007 for 52 Ma, and 0.639 ± 0.010 for 53 Ma (95% confidence levels, shown in Figure 3.1A). The average Δ_{47} of the background conditions of the ETM-2 was 0.633 ± 0.006 (Agterhuis, Ziegler, and Lourens, *in pre-print*). External reproducibility of the Δ_{47} of ETH-3 after corrections was 0.023‰ , and that of $\delta^{18}\text{O}$ and $\delta^{13}\text{C}$ were 0.138‰ and 0.104‰ , respectively. All standard deviations of the ETH-1, 2 and 3 standards measurements are shown in Table 3.1.

The resulting benthic temperatures are $14.31 \pm 3.05\text{°C}$ for 48 Ma, $19.60 \pm 3.13\text{°C}$ for the EECO (51 Ma), $17.00 \pm 2.35\text{°C}$ for 51.5 Ma, $15.27 \pm 2.32\text{°C}$ for 52 Ma, $12.38 \pm 3.15\text{°C}$ for 53 Ma, and $13.98 \pm 2.05\text{°C}$ for the background of ETM-2 (95% confidence levels, fully propagated). Given the average temperatures, a warming of $\sim 7.22 \pm 4.44\text{°C}$ occurred between 53 Ma and the EECO (51 Ma) in approximately 2 Myr. Interpolating between the EECO and 48 Ma, the deep sea cooled with $\sim 5.29 \pm 4.37\text{°C}$ in 3 Myr.

The calculated temperatures appear to follow the general trends of the $\delta^{18}\text{O}$ of Lauretano, Zachos, and Lourens (2018). An exception is 53 Ma, which is cooler than expected, especially given the associated average $\delta^{18}\text{O}$ (panels B and C, Figure 3.1).

Following the clumped isotope temperatures, an independent value for $\delta^{18}\text{O}_w$ could be calculated according to equation 2.5 in the Materials and methods section, see panel D in Figure 3.1. The warmest clumped temperatures yield positive $\delta^{18}\text{O}_w$, exceeding the present-day value of 0‰ VSMOW, and only 53 Ma falls on the value of -0.98‰ VSMOW previously assumed for the Eocene.

Table 3.1: Standard deviations of the ETH-standards.

Standard	Δ_{47}	$\delta^{18}\text{O}$	$\delta^{13}\text{C}$
ETH-1 (N=19)	0.049	0.133	0.082
ETH-2 (N=19)	0.033	0.148	0.070
ETH-3 (N=95)	0.023	0.138	0.104

Deep ocean temperatures from an early Eocene clumped isotope record

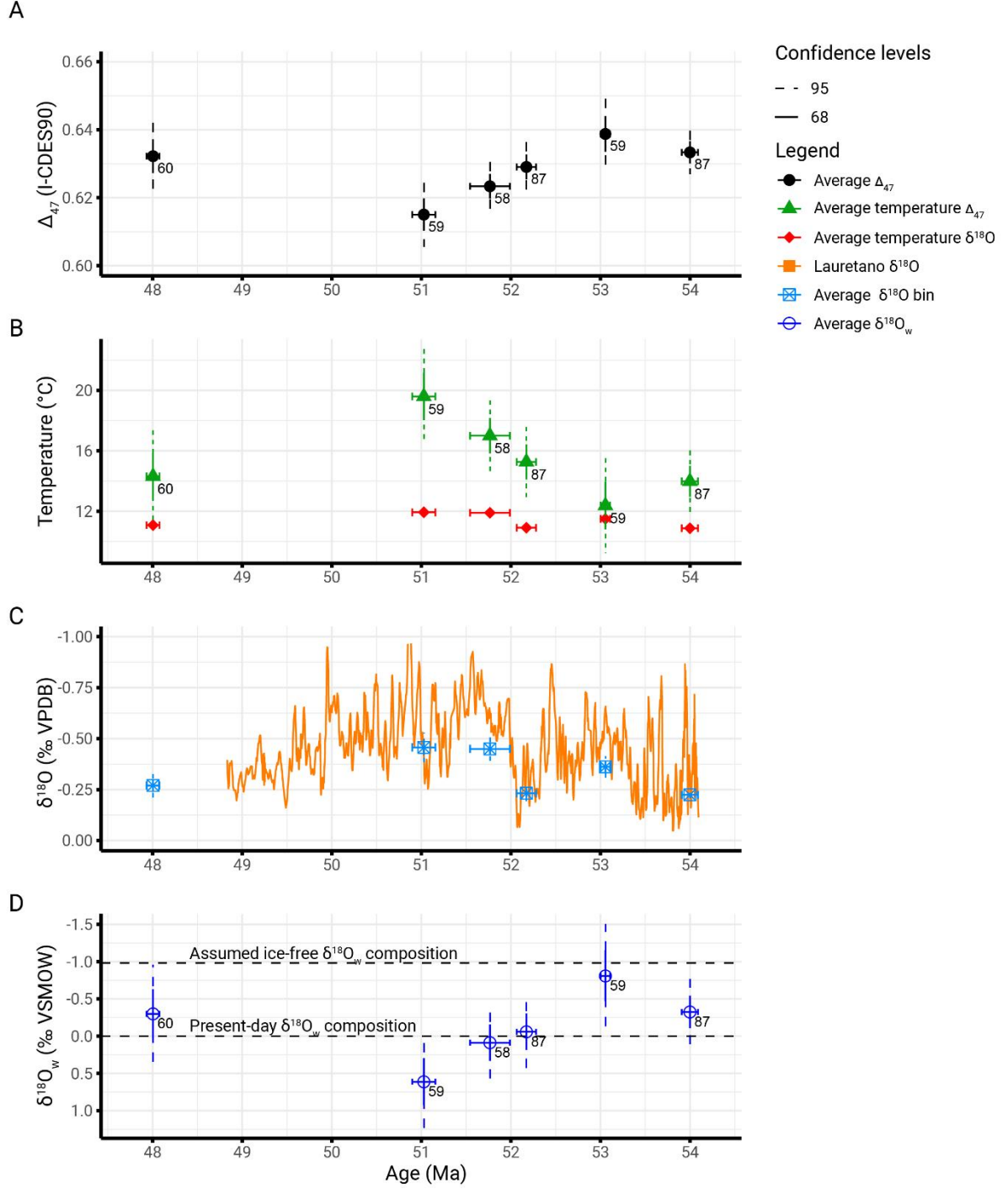


Figure 3.1: Compilation of stable isotope data and calculated temperatures. Temporal ranges are indicated by the horizontal error bars, confidence levels are indicated by the vertical error bars. A: Δ_{47} values of all bins with the amount of measurements included. B: The temperatures as calculated for the Δ_{47} bins using the Meinicke et al. (2021) calibration, and temperatures for the $\delta^{18}\text{O}$ assuming a $\delta^{18}\text{O}_w$ of -0.98 ‰ VSMOW using the Marchitto et al. (2014) calibration. C: $\delta^{18}\text{O}$ record of Lauretano, Zachos, and Lourens (2018) using a rolling mean, alongside the average $\delta^{18}\text{O}$ of the Δ_{47} measurements. D: The calculated $\delta^{18}\text{O}_w$ values using the Marchitto et al. (2014) calibration with horizontal lines for comparison to previous assumptions of the Eocene (Zachos, Stott, and Lohmann 1994) as well as the value for present day.

4. Discussion

4.1. Deep ocean temperatures as derived from Δ_{47} , $\delta^{18}\text{O}$, and Mg/Ca

A comparison between average Δ_{47} , $\delta^{18}\text{O}$, and Mg/Ca-derived temperatures of Cramer et al. (2011) is shown in Figure 4.1. The Mg/Ca dataset uses two calibrations, one based upon Lear, Mawbey, and Rosenthal (2010), the other based upon Rathmann et al. (2004). Both calibrations were established using *Oridorsalis umbonatus* but differ significantly in their Mg/Ca to temperature slopes, the reason for which is unknown (Cramer et al. 2011).

A substantial offset between $\delta^{18}\text{O}$, and Δ_{47} as well as Mg/Ca-temperatures is evident. This is ingrained of the low variance in benthic $\delta^{18}\text{O}$ ($\delta^{18}\text{O}_b$), ranging from -0.46‰ to -0.22‰. Given the temperature relation from Marchitto et al. (2014) and the Mg/Ca & Δ_{47} -temperatures, this means that high discrepancies result from the assumptions used in the $\delta^{18}\text{O}$ -temperature proxy. In general, both Mg/Ca and Δ_{47} -temperatures are at least 3 °C higher than $\delta^{18}\text{O}$ averages, except for 53 Ma where the three proxies are in close proximity. As opposed to Agterhuis et al. (*in pre-print*), Δ_{47} -temperatures are not necessarily consistently higher than Mg/Ca temperatures (Figure 4.1).

A part of the discrepancies could be explained by the so-called ‘pH effect’. Seawater pH is inversely related to $\delta^{18}\text{O}_b$ (Ravelo and Hillaire-Marcel 2007; Zeebe et al. 2008; Uchikawa and Zeebe 2010). Unfortunately, the pH effect has not yet been quantified for benthic foraminifera (Uchikawa and Zeebe 2010), with the exception of one core-top study after *Oridorsalis umbonatus*, but which resulted in inconclusive evidence (Rathmann and Kuhnert 2008). Nevertheless, a pH correction is attempted here, using the pH-relationship of Zeebe (1999, 2001) and a pH record by Rae et al. (2021). The pH-corrected $\delta^{18}\text{O}_b$ can be calculated by using a slope of 1.42 ‰/unit pH (Zeebe 2001), and assuming no pH-correction at pH 8 (Meckler et al., *in pre-print*). The resulting pH-corrected $\delta^{18}\text{O}_b$ are then used to obtain new temperatures. However, given the large uncertainties in pH and biotic problems as mentioned above, the pH effect should be considered mostly for illustration. The pH effect is discussed further in section 4.3 below.

Although the Δ_{47} -data is limited in resolution, an agreement in temperature evolution can be observed when comparing to Mg/Ca temperatures. However, absolute numbers are divergent. Strictly speaking, the Δ_{47} -temperature error margins fall within the 90% error margins of the Mg/Ca temperatures of Cramer et al. (2011), though this correlation would be unlikely. Moreover, a cooling between 52 and 51 Ma in Mg/Ca is not visible in the Δ_{47} -temperatures. Remarkably, previous comparisons of Δ_{47} and Mg/Ca temperature studies found good agreement (Evans et al. 2018; Modestou et al. 2020; Meinicke et al. 2021), although these are focussed on either sea surface temperatures, or more recent epochs.

There is a variety of assumptions and uncertainties in Mg/Ca-derived temperatures that could explain the absolute discrepancies and pattern offsets. Firstly, the Mg/Ca of the seawater ($\text{Mg}/\text{Ca}_{\text{sw}}$) varies over time. $\text{Mg}/\text{Ca}_{\text{sw}}$ fluctuates over timescales of millions of years due to the composition and flux of riverine input, changes in the precipitation of dolomite over carbonate, and the rate of ocean crust

production (Evans and Müller 2012). For example, $\text{Mg}/\text{Ca}_{\text{sw}}$ was only ~ 2 mol/mol during the Paleogene, whereas it is over ~ 5 mol/mol today (Coggon et al. 2010). These secular changes need to be corrected for, as they are independent of ocean temperature. Secondly, benthic foraminifera species show different temperature sensitivities, represented by the exponent H in the Mg/Ca calculations. The dataset of Cramer et al. (2011) used here has utilized a series of different exponents depending on benthic foraminifera species. The exponent H also includes the $\delta^{18}\text{O}$ of seawater ($\delta^{18}\text{O}_{\text{w}}$), which must be assumed for the presumably ice-free Eocene. Thirdly, benthic foraminifera Mg/Ca also reflect the gradient in the dissolved carbonate concentration $\Delta[\text{CO}_3^{2-}]$, which varies over ocean depth (Elderfield et al. 2006). Lastly, there appears to be a very sparse amount of data for the Eocene in the Cramer et al. (2011) dataset (see Figure S1 of the Cramer et al. 2011 supplement). Smoothing of such sparse data may lead to aliasing effects, in which long-term trends are inferred from short-scale variations. This means that the resolution of the Mg/Ca data as presented there is perhaps insufficient for single million-year scale variations (Cramer et al. 2011).

Altogether, Mg/Ca is strongly influenced by an assortment of uncertainties, which may be less well constrained for the Eocene than other coupled Δ_{47} and Mg/Ca studies have been able to resolve for more recent epochs. In fact, this difference could be used to better constrain the Mg/Ca proxy. For instance, the independency of Δ_{47} allows calculation of the secular variations in $\text{Mg}/\text{Ca}_{\text{sw}}$ chemistry

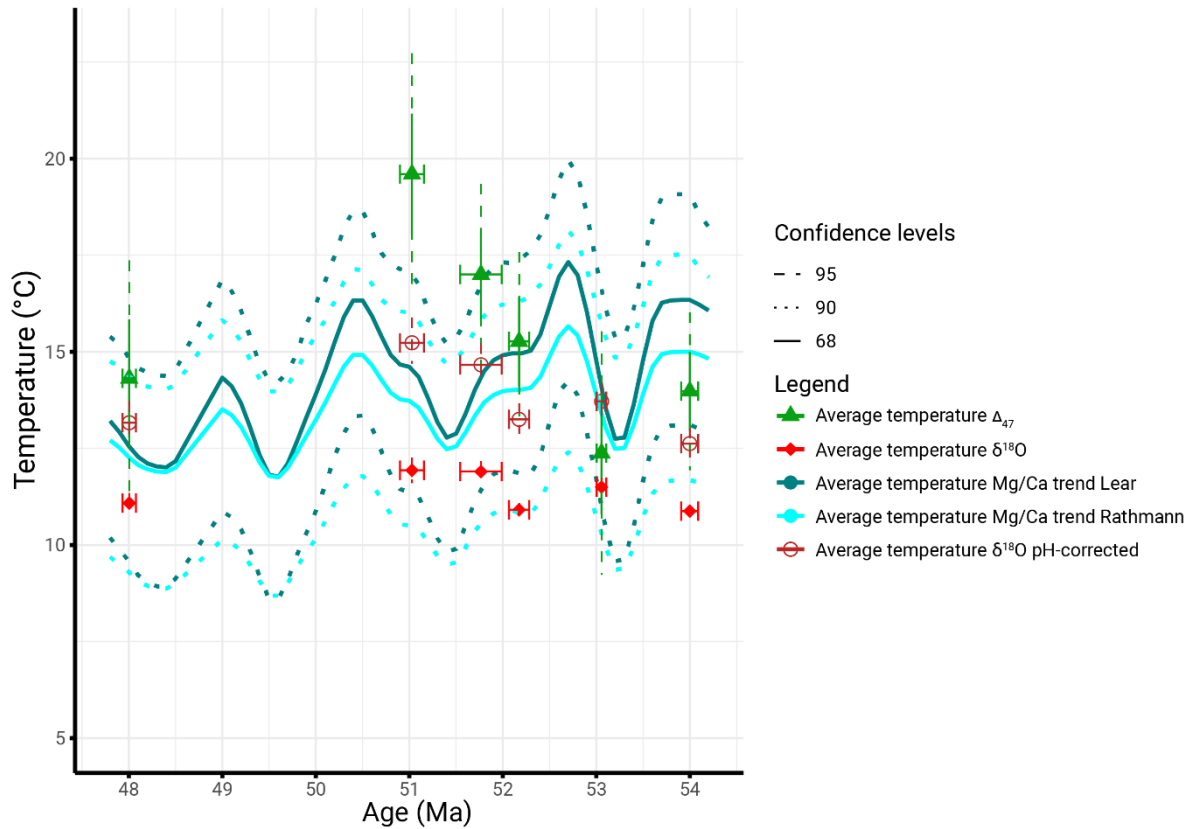


Figure 4.1. Comparison of temperatures as calculated from the average Δ_{47} , $\delta^{18}\text{O}_{\text{b}}$ (green and red respectively, this study), and Mg/Ca of Cramer et al. (2011) using the linear calibrations of Lear, Mawbey, and Rosenthal (2010) in teal and Rathmann et al. (2004) in cyan. Dark-red, open circles indicate the pH-corrected estimates of $\delta^{18}\text{O}_{\text{b}}$.

(Evans et al. 2018). This in the end enables refinement of Mg/Ca thermometry, if the errors on Δ_{47} can be minimized.

4.2 The $\delta^{18}\text{O}_w$ composition of deep waters

Temperature proxies that are independent of $\delta^{18}\text{O}_b$ allow the calculation of $\delta^{18}\text{O}_w$ of the past oceans (see Methods section 2.3.4). The calculated $\delta^{18}\text{O}_w$ values for Δ_{47} temperatures, alongside Mg/Ca calculated $\delta^{18}\text{O}_w$ values, are shown in Figure 4.2. For the Δ_{47} temperatures, both regular $\delta^{18}\text{O}_w$ and pH effect corrected $\delta^{18}\text{O}_w$ have been plotted. The pH-corrected $\delta^{18}\text{O}_w$ were obtained by using the pH-corrected $\delta^{18}\text{O}_b$ from section 4.1, using the Δ_{47} -temperatures. The confidence levels include the errors of $\delta^{18}\text{O}_b$, seawater pH, and the Δ_{47} -temperatures.

At the warmest temperatures (51 and 51.5 Ma), $\delta^{18}\text{O}_w$ exceeds the present-day value of 0‰ VSMOW, while Mg/Ca derived $\delta^{18}\text{O}_w$ floats around -1‰. Only the Δ_{47} -obtained $\delta^{18}\text{O}_w$ of 53 Ma falls around the value of -0.98‰ VSMOW, previously assumed for the ice-free early Eocene (Zachos, Stott, and Lohmann 1994). The pH effect corrected Δ_{47} -values are closer to Mg/Ca-derived $\delta^{18}\text{O}_w$, with all points overlapping within the confidence intervals. Note that the Mg/Ca $\delta^{18}\text{O}_w$ -values have already been pH-corrected with 0.7‰ by Cramer et al. (2011).

As described in section 4.1, the average $\delta^{18}\text{O}_b$ shows very little variance. While using the Marchitto et al. (2014) equation for temperature, and assuming $\delta^{18}\text{O}_w = -0.98‰$ VSMOW, variance in temperature will inherently follow that of $\delta^{18}\text{O}_b$, meaning very constant temperatures. Calculating $\delta^{18}\text{O}_w$ using the same relationship, however, means that $\delta^{18}\text{O}_w$ will be entirely temperature-dominated when variance in $\delta^{18}\text{O}_b$ is minimal, as is evident from Figure 4.2.

Discrepancies between the Δ_{47} temperature and Mg/Ca temperature-derived $\delta^{18}\text{O}_w$ values are not readily explained. Using the fact that Δ_{47} temperatures are independent of the assumptions made for Mg/Ca, the likelihood of Δ_{47} -derived $\delta^{18}\text{O}_w$ to be accurate is more plausible (Evans 2021 and references therein). This leaves a conundrum concerning the source of the isotopically different values, however. If the Earth was essentially ice-free in the early Eocene, then what mechanism drove $\delta^{18}\text{O}_w$ towards isotopically heavier compositions?

It may well be that the Eocene was not entirely ice-free, and that a dynamic cryosphere was present in at least the middle to late Eocene (Tripathi et al. 2005; Miller, Wright, and Browning 2005). There is a $+1.42 \pm 0.95$ ‰ change between 53 Ma and the EECO (51 Ma), however, which is in the order of the Pleistocene cryosphere changes (e.g. Lisiecki and Raymo 2005), which is associated with 120–130 m sea-level change. Eustatic sea-level records do not show changes of that magnitude for the Early Eocene (Miller et al. 2020).

The presence of greenhouse-world ice sheets and their potential extent are still highly debated. Modelling and sea-level records show that ice sheets of 40 m sea-level equivalent may have been present (Miller, Wright, and Browning 2005). Moreover, ice sheets 60% the size of the Pleistocene have been proposed for the ultimate greenhouse of the Turonian (Cretaceous, 93.5–89.3 Ma) as indicated by $\delta^{18}\text{O}$ (Bornemann et al. 2008). Others claim that extant ephemeral ice sheets may have developed only as early as the termination of the EECO, based upon CO_2 thresholds and astronomical parameters (Pearson and Palmer 2000; Westerhold and Röhl 2009). It is likely that ice sheets can explain changes in $\delta^{18}\text{O}_w$, but only to a limited degree (Miller et al. 2020).

An alternative to glacio-eustasy as the primary driver of fluctuations in $\delta^{18}\text{O}_w$ is aquifer-eustasy (Wendler et al. 2016; Sames et al. 2020). Aquifer-eustasy involves long-term storage of meteoric water as groundwater, at sea-level change magnitudes. The charging or discharging of these reservoirs depend on the intensity of the hydrological cycle, and thus climate. Using Rayleigh distillation, the same mechanisms as for ice sheets, these reservoirs will be relatively depleted in $\delta^{18}\text{O}$ compared to the ocean

(Agterhuis et al., *in pre-print*). Eustatic sea-level change as a result of groundwater charging and discharging has been found to be limited to 5 metres in the most optimistic scenarios, however, insufficient to explain $+1.42 \pm 0.95$ ‰ change in $\delta^{18}\text{O}_w$ (Davies et al. 2020), even when combined with potential ice-sheets.

Further possibilities for fluxes in $\delta^{18}\text{O}_w$ are seafloor spreading and mantle output at subduction zones. Hydrothermal activity and volcanic water emissions at subduction zones emit ^{18}O , causing significant changes in $\delta^{18}\text{O}_w$ over the geologic past (Wallmann 2001). Moreover, seafloor spreading, and thus ^{18}O -input, has been found to increase halfway through the Cenozoic according to both tectonics and astronomical time scale calibration (Conrad and Lithgow-Bertelloni 2007; Westerhold et al. 2017). Nevertheless, these tectonic changes in ^{18}O -input are on a 10-to-100-million-year scale and are difficult to reconcile on a single million-year scale, which is the resolution in this study.

Finding similar discrepancies when comparing $\delta^{18}\text{O}_w$ between records in the Miocene, Modestou et al. (2020) somewhat speculatively propose spatial patterns in salinity, and thus $\delta^{18}\text{O}_w$. Yet, Evans (2021) suggests that a larger Miocene ice sheet could also be responsible, as ice sheet models are able to reconstruct similar $\delta^{18}\text{O}_w$ -values. In addition, large spatial salinity patterns require an absence of

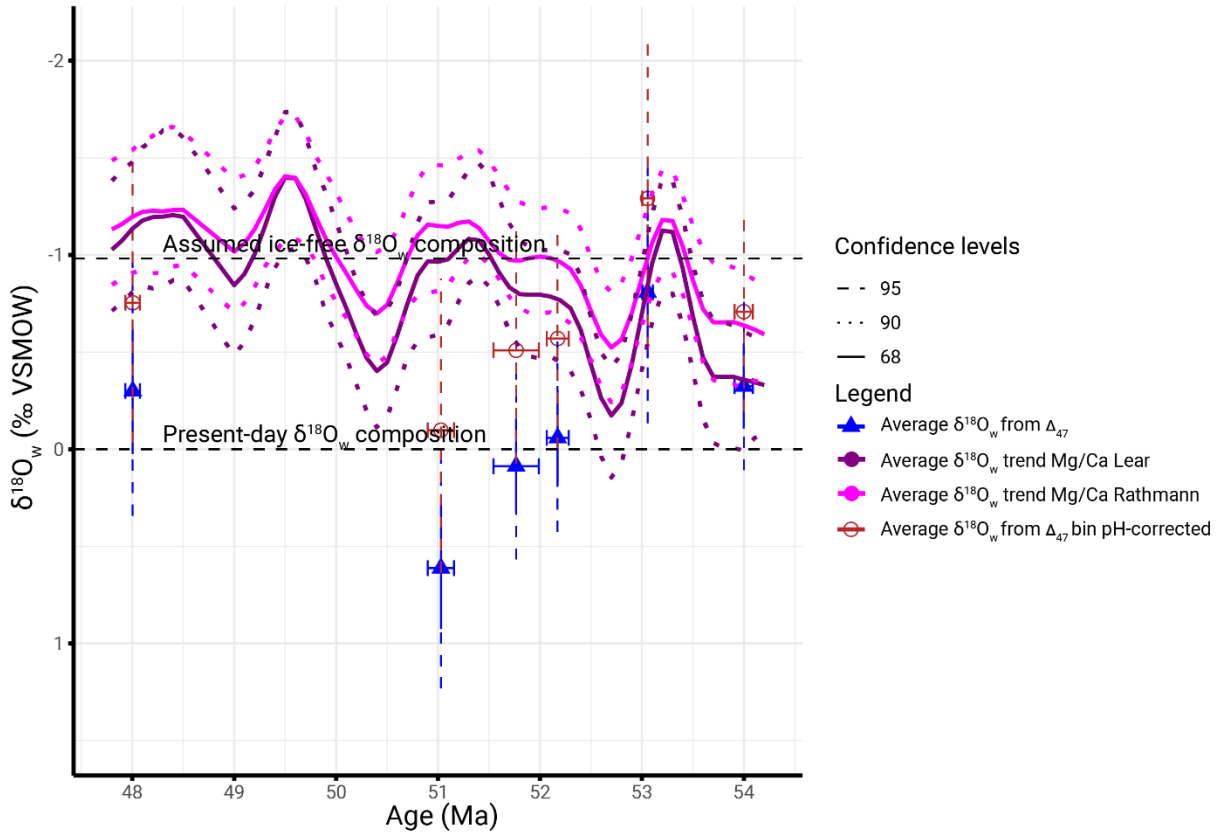


Figure 4.2: Comparison of $\delta^{18}\text{O}_w$ for Δ_{47} (this study), and the $\delta^{18}\text{O}_w$ of Cramer et al. (2011) using the linear calibrations of Lear, Mawbey, and Rosenthal (2010) in purple and Rathmann et al. (2004) in magenta. Horizontal lines indicate the assumed ice-free $\delta^{18}\text{O}_w$ composition of the Eocene and the present-day value for $\delta^{18}\text{O}_w$. Dark-red, open circles indicate estimates of $\delta^{18}\text{O}_w$ using a pH-corrected $\delta^{18}\text{O}_b$ with Δ_{47} -temperatures.

circulation. Yet, the Neodymium circulation proxy (ϵ_{Nd}) suggests that Atlantic meridional overturning circulation intensified in the Palaeogene (Batenburg et al. 2018), which would homogenize deep waters. At present, no clear mechanisms stand out as to explain the early Eocene $\delta^{18}O_w$.

4.3 The pH effect of $\delta^{18}O_b$ and Δ_{47}

As mentioned in section 4.1, $\delta^{18}O_b$ is raised with declining seawater pH. The intensity of the pH effect has only been established for modern planktic foraminifera in cultivation studies (Spero et al. 1997; Bijma, Spero, and Lea 1999). It has been suggested to be applicable to planktic and benthic foraminifera alike (Spero et al. 1997; Zeebe 2001; Rathmann and Kuhnert 2008), although the effect remains poorly constrained for benthic foraminifera (Uchikawa and Zeebe 2010). In Figures 4.1 and 4.2, a pH effect of 1.42 ‰/unit pH was used (Zeebe 2001). As described by Uchikawa and Zeebe (2010), the validation of this pH-effect is based upon of Spero et al. (1997), using a twofold of assumptions: (1) the pH effect of modern planktic foraminifera is universal, and (2) the empirical data of Spero et al. (1997) is also applicable to the more acidic seas of the Eocene. Additionally, the pH-values used for the pH corrections were taken from planktic foraminifera (Rae et al. 2021), and it is assumed here that the deep ocean will have the same seawater pH. However, circulation and other local effects can influence deep water pH to be different from the surface ocean (Rae 2018). Still, given these intrepid assumptions, it should be noted that the purpose of this exercise is illustrative, and not quantitative. More work on quantifying the pH effect of benthic foraminifera is required.

It has been suggested that Δ_{47} suffers the same influences of the pH effect, in the same direction as $\delta^{18}O_b$ (Tripathi et al. 2015), though the effects are limited (Kluge et al. 2018; Guo 2020), and negligible for at least the pH of typical seawater (Kele et al. 2015).

4.4 Sea surface – deep ocean mismatch

The deep ocean warming of $\sim 7.22 \pm 4.44$ °C between 53 Ma and the EECO at Walvis Ridge is significant when put into a global context. Sea surface temperatures (SST) raised a maximum of ~ 4 °C for the same time period in Siberia (Frieling et al. 2014), and other high-latitude sites such as ODP 1172 (Tasmania) and IODP U1356 (Southern Ocean) raised by only ~ 2 °C or even lowered slightly, as shown in Figure 4.3A. The cooling after the maximum of the EECO is evident for most of the SST records. Interestingly, the SSTs of Siberia appear to lead the deep ocean. This could be caused by inaccuracies in the age model, which was built using magnetostratigraphy and dinocyst assemblage zones, and is subject to some hiatuses (Frieling et al. 2014 supplement). The deep ocean warming is well reflected in the atmospheric CO_2 proxy record, which nearly doubles over the interval (Figure 4.3B).

It is striking that sea surface temperatures stayed relatively constant over the course of the EECO, and that the deep ocean did not, especially considering the CO_2 pattern. This is in direct disagreement with the classical view of the deep ocean, which should reflect long-term surface conditions, and is found to evolve synchronously, such as in Cramwinckel et al. (2018). They utilize $\delta^{18}O_b$ directly as a temperature proxy to feed the deep-ocean boundary conditions for a general circulation model (GCM), which is used to quantify polar amplification across the Eocene, and calculate predicted SSTs that match with their TEX_{86} estimations. Given the mismatch of $\delta^{18}O_b$ and Δ_{47} -temperatures, however, means the outcome for TEX_{86} SSTs using this approach are likely also offset. The new Δ_{47} -temperatures as presented here might mean that previous estimates of polar amplification need re-evaluating, and that changes in surface temperatures cannot be reliably obtained from deep ocean temperatures for at least the early Eocene.

TEX_{86} SSTs are pestered by a variety of issues, as mentioned in section 1.2. The unmoving SSTs in Figure 4.3A could specifically be the result of calibration insensitivity for the surface conditions of the

Deep ocean temperatures from an early Eocene clumped isotope record

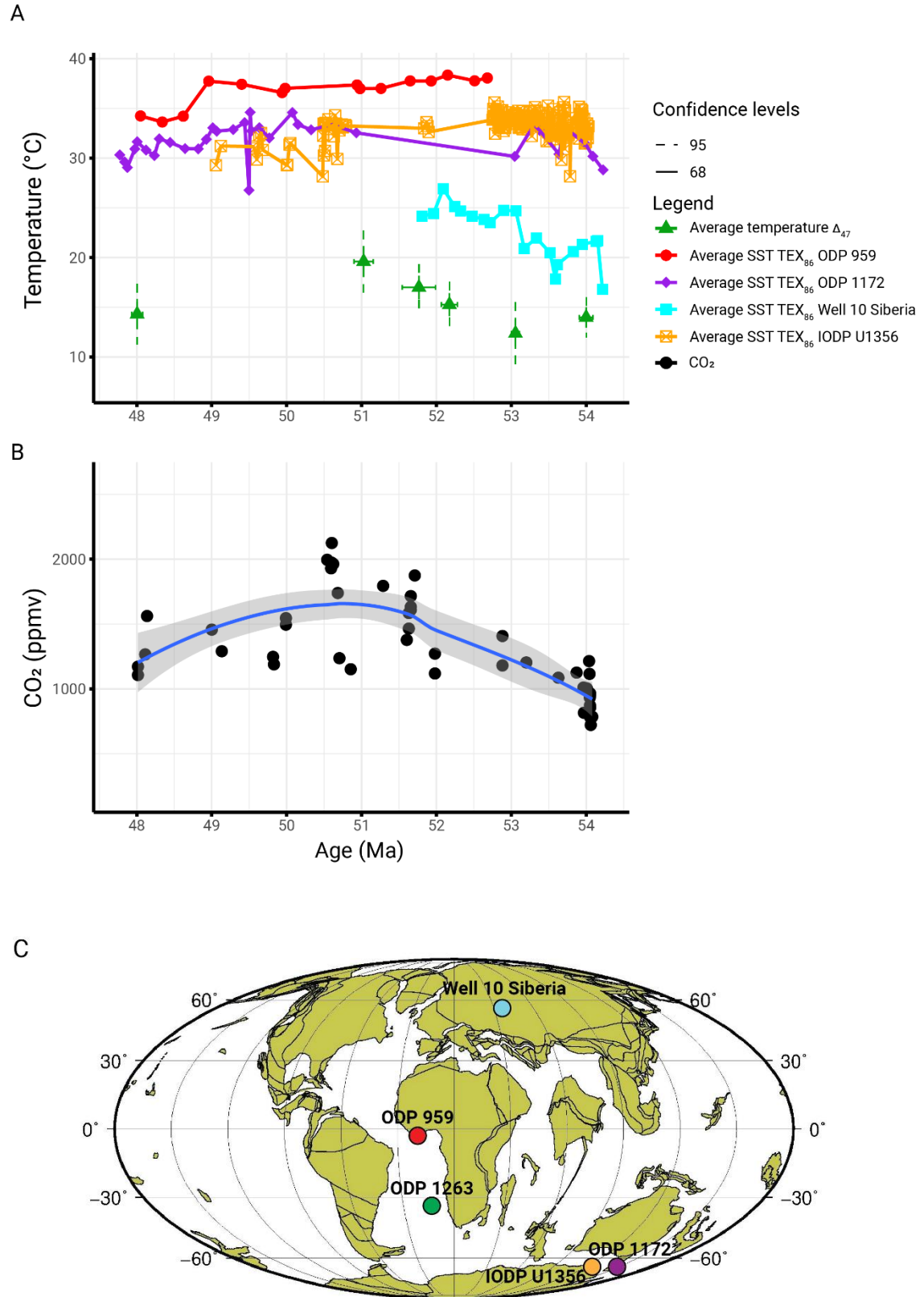


Figure 4.3. A: Sea surface and deep ocean temperatures. Sea surface temperatures are taken from the compilation of TEX₈₆ data of Hollis et al. (2019), and are originally from Cramwinckel et al. (ODP Site 959, 2018), Bijl et al. (ODP Site 1172, 2009), Frieling et al. (Siberia, 2014), and Bijl et al. (IODP Site U1356, 2013). The TEX₈₆ temperatures were calculated by Hollis et al. (2019) using the Bayesian regression calibration (BAYSPAR) of Tierney and Tingley (2015). Deep ocean Δ_{47} -temperatures are from this study. The temperatures

for both the sea surface and the deep ocean are plotted on the same axis for direct comparison. B: CO₂ record from borate in foraminifera by Rae et al. (2021). The blue line is a locally weighted polynomial (LOESS), with grey shading indicating 95% confidence. C: Palaeogeographic map (50 Ma) showing the location of the various sites that are included, made using <https://www.odsn.de/odsn/services/paleomap/paleomap.html> after Hay et al. (1999).

EECO. TEX₈₆ calibrations are based upon modern SSTs, which are limited to a maximum temperature of ~30 °C, meaning that any higher temperature will have to be extrapolated (Hollis et al. 2012). However, the mathematical relation above the modern ~30 °C limit is unknown and therefore paleotemperatures of the Eocene and Cretaceous should be taken with caution (Dunkley Jones et al. 2020; Hollis et al. 2019). Unfortunately, other SST proxies are scarce due to the lacking preservation of carbonates (Hollis et al. 2019).

4.5 Circulation and water masses

The heavy values for $\delta^{18}\text{O}_w$ during the peak of the EECO may resemble a switch in source waters for the deep ocean. Rather than forming heavy $\delta^{18}\text{O}_w$ deep waters due to an extensive ice sheet cover, as in the Pleistocene, it could be the case that saline water from the tropics dominated the deep ocean. Warm, saline deep-waters will give comparable $\delta^{18}\text{O}_b$ -signatures to cold high-latitude sourced deep-waters. $\delta^{18}\text{O}_b$ could thus be considered a density proxy (Lynch-Stieglitz, Curry, and Slowey 1999).

Ocean circulation has been proposed to reverse (as mentioned above) under the extreme greenhouse world of the PETM, according to an atmosphere-ocean GCM (AOGCM) study (Lunt et al. 2010), and Mg/Ca and $\delta^{13}\text{C}$ comparisons (Tripathi and Elderfield 2005; Nunes and Norris 2006). When atmospheric carbon-dioxide (CO₂) is low, high-latitude sea ice cools the surface waters, and brine rejection adds density, resulting in the sinking of these waters. When CO₂ is high, as during the PETM, the source may switch to the lower latitudes, where high rates of evaporation forms intermediate waters with high-salinity, and thus high $\delta^{18}\text{O}_w$ (Huber and Sloan 2001; Tripathi and Elderfield 2005; Lunt et al. 2010). Atmospheric carbon-dioxide concentrations of the EECO were very similar to that of the PETM, if not higher (Rae et al. 2021).

Tripathi and Elderfield (2005) suggest that potentially increased precipitation at high-latitudes lowered salinity (and $\delta^{18}\text{O}_w$), and thus density in the Southern Ocean. Rather, deep water formed at the low-latitude Pacific Ocean, since both the Atlantic and Southern Oceans freshened in $\delta^{18}\text{O}_w$. Yet, this is based upon Mg/Ca temperatures which were uncorrected for pH. Evans et al. (2016) demonstrates that pH will have a significant effect on the outcome of $\delta^{18}\text{O}_w$ from Mg/Ca temperatures, which would under the pH conditions of the PETM neutralize the freshening that Tripathi and Elderfield (2005) observed for the Southern Ocean and the Atlantic Ocean. While models and proxies do indicate higher precipitation for the PETM as well as the early Eocene (Carmichael et al. 2016, 2017, and references therein), changes in circulation based upon their Mg/Ca derived $\delta^{18}\text{O}_w$ should be taken sensibly. The heavy $\delta^{18}\text{O}_w$ from Δ_{47} -temperatures as found in this study makes the low-latitude Atlantic appear more plausible as a deep water source, in line with Lunt et al. (2010).

In contrast to the reversed circulation as suggested above, more recent model studies show that deep-water formation was still focussed in the Southern Ocean, despite any potential salinity changes (Zhang et al. 2020; Lunt et al. 2021). In fact, high-salinity, heavy $\delta^{18}\text{O}_w$ subtropical waters may have been advected to the subpolar gyres of the Southern Ocean (salt-advection feedback, Ferreira et al. 2018), where deep water convection occurred (Zhang et al. 2020). Moreover, Zhang et al. (2020) find that precipitation is lowered in the Southern Ocean, in contrast with the reversed circulation model. Instead, they suggest that precipitation increased in the Northern Pacific Ocean along the paleo-Rockies, which inhibits deep water formation and would lower $\delta^{18}\text{O}_w$ locally. Picking either of these opposing views of

circulation cannot be done based on the evidence presented in this study alone. Future work could focus on tracing the source of the deep waters, for example by making a Southern Ocean and a Northern Pacific Δ_{47} -record, so that the circulation dichotomy between proxy and model can be resolved.

4.6 Global mean surface temperature and climate sensitivity

The differences between the $\delta^{18}\text{O}_b$ and Δ_{47} -temperatures have major implications for previous estimates of global mean surface temperature (GMST) and climate sensitivity. Recent approximations for GMSTs and climate sensitivity are based upon $\delta^{18}\text{O}_b$ temperatures (Inglis et al. 2020), and may therefore underestimate the actual GMSTs, given the complications in $\delta^{18}\text{O}_b$ as mentioned earlier. Consequently, new values for GMST and climate sensitivity can be calculated using our Δ_{47} -temperatures, following the outline of Inglis et al. (2020).

GMST changes prior to the Pliocene can be assumed to follow the changes in the bottom water temperature ($\Delta BWT = \Delta GMST$, Hansen et al. 2013). The earliest Pliocene conditions are used to determine the early Eocene GMST, in accordance with Hansen et al. (2013) and Inglis et al. (2020):

$$(4.1) \quad GMST_{EE} - GMST_{Pliocene} = BWT_{EE} - BWT_{Pliocene}$$

- Where $GMST_{EE}$ and $GMST_{Pliocene}$ are the global mean surface temperatures for the early Eocene and Pliocene respectively;
- Where BWT_{EE} and $BWT_{Pliocene}$ are the bottom water temperatures for the early Eocene and the Pliocene respectively.

To obtain the $GMST_{Pliocene}$, equation 4.2 from Hansen et al. (2013) can be used, which combined with the above results in the following equation:

$$(4.2) \quad GMST_{EE} = (2.5 \times BWT_{Pliocene} + 12.15) + (BWT_{EE} - BWT_{Pliocene})$$

$BWT_{Pliocene}$ is set at 2.0 °C (Hansen et al. 2013), and the Δ_{47} -temperatures are used for BWT_{EE} . Due to the different early Eocene boundary conditions, the estimates need to be corrected for by 3-5 °C to compensate for non- CO_2 effects like aerosols, vegetation, and paleogeography (Lunt et al. 2021). Therefore, 4.0 °C was subtracted linearly from the GMST estimates, and the extremes of 3 and 5 °C have been included in the error margins. The resulting GMST estimates are plotted in Figure 4.4A. The EECO has a GMST of 34.9 ± 4.1 °C (95% confidence levels). In comparison, Inglis et al. (2020) report a GMST of 28 ± 1.30 °C (68% confidence level) using their $\delta^{18}\text{O}_b$ deep ocean temperature dataset (D_{deep}). Thus, Δ_{47} -temperatures yield a higher EECO GMST.

Using the GMSTs, an Equilibrium Climate Sensitivity (ECS) can now be obtained. The ECS is defined as ‘the equilibrium change in global near-surface air temperature resulting from a doubling in atmospheric CO_2 ’ (Inglis et al. 2020). The CO_2 forcing compared to the pre-industrial conditions can be calculated with the simplified radiative forcing fit for CO_2 from Byrne and Goldblatt (2014):

$$(4.3) \quad \Delta F_{\text{CO}_2} = 5.32 \ln\left(\frac{C_{EE}}{C_{PI}}\right) + 0.39[\ln\left(\frac{C_{EE}}{C_{PI}}\right)]^2$$

- Where ΔF_{CO_2} is the change in radiative forcing due to CO_2 ;
- Where C_{EE} and C_{PI} are the CO_2 conditions for the early Eocene and pre-industrial, respectively.

The CO_2 values for the early Eocene bins were taken from Rae et al. (2021), and the CO_2 of the pre-industrial was set at 278 ppm, following Inglis et al. (2020). Finally, to get to the ECS for the early Eocene, equation 2 of Anagnostou et al. (2016) can be used:

$$(4.4) \quad ECS = \frac{\Delta GMST_{EE \text{ vs } PI}}{\Delta F_{\text{CO}_2}}$$

- Where $\Delta GMST_{EE \text{ vs } PI}$ is the change in temperature due to CO_2 of the early Eocene compared to the pre-industrial.

The resulting ECS values have been plotted in Figure 4.4B. The ECS of the EECO is $6.0\text{ }^{\circ}\text{C}/2\times\text{CO}_2$, with a maximum of 9.1 and a minimum of $4.1\text{ }^{\circ}\text{C}/2\times\text{CO}_2$. In comparison, using the deep ocean-derived GMST of Inglis et al. (2020) to calculate an ECS results in $5.0\text{ }^{\circ}\text{C}/2\times\text{CO}_2$, with a maximum of 6.5 and a minimum of $4.2\text{ }^{\circ}\text{C}/2\times\text{CO}_2$ (95% confidence levels). The Δ_{47} -temperature gives $1.0\text{ }^{\circ}\text{C}$ more warming per doubling of CO_2 , and has a much higher maximum, meaning that $\delta^{18}\text{O}_b$ temperatures lead to underestimations of ECS. This is in agreement with climate model simulations by Zhu, Poulsen, and Tierney (2019) that are modified to better capture cloud-feedback mechanisms. They find that cloud microphysics may play an important role in shortwave radiation feedbacks. At warmer climate states, cloud droplets increase in size, which makes them less opaque. This focuses their scattering of shortwave radiation forward, increasing the shortwave radiation reaching the Earth's surface. Moreover, a reduction in cloud cover also increases incoming shortwave radiation (Zhu, Poulsen, and Tierney 2019). Following these results, climate states appear to be important for the magnitude of climate sensitivity, in line with previous findings based on Mg/Ca temperatures and $\delta^{11}\text{B}$ CO_2 estimates (Anagnostou et al. 2020).

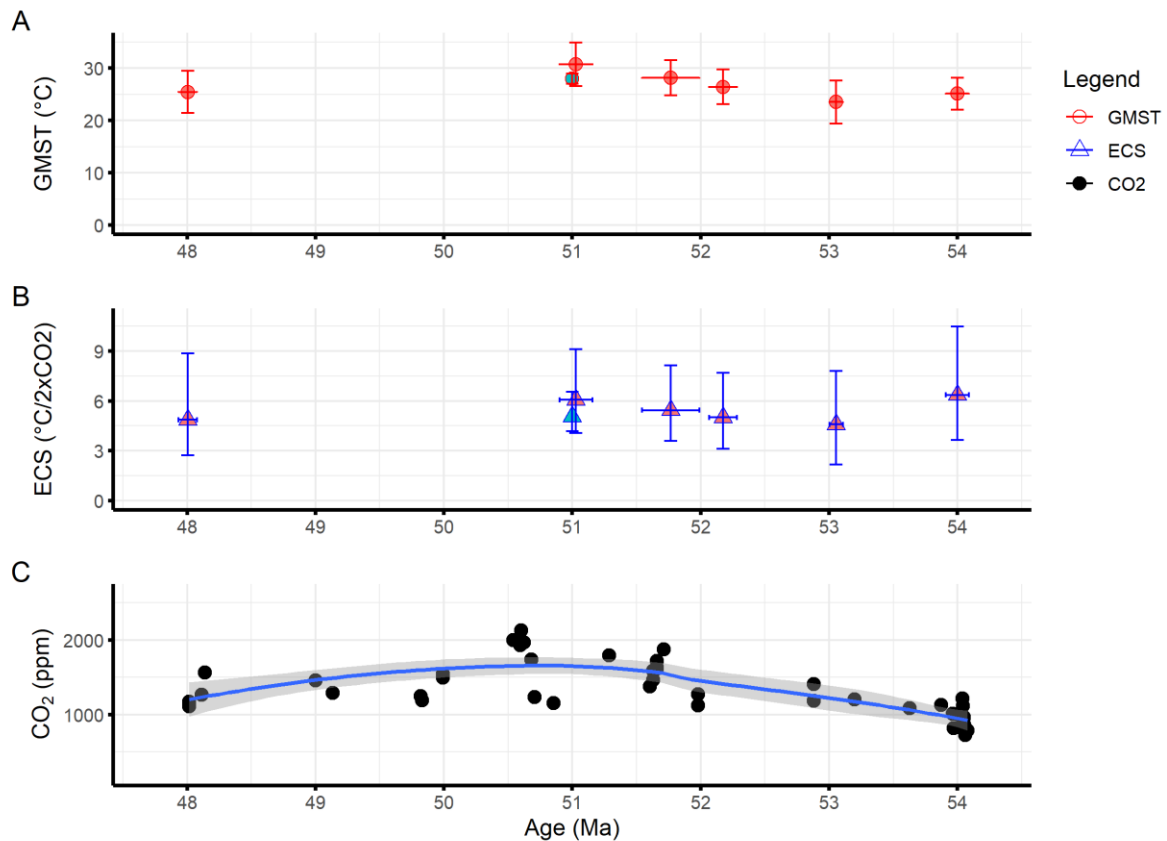


Figure 4.4 A: GMSTs over the early Eocene (95% confidence levels), including the GMST as calculated by Inglis et al. (2020) for the EECO using their deep sea dataset (51 Ma, cyan-filled shapes, 68% confidence level). B: ECS from this study and one point from Inglis et al. (2020, all 95% confidence levels). Note that the errors are asymmetrical due to the CO_2 data of Rae et al. (2021). C: CO_2 record from Rae et al. (2021) with a LOESS regression (blue line) with shaded regions indicating 95% confidence levels.

5. Conclusions

A clumped isotope (Δ_{47}) temperature record of the early Eocene is presented, which reveals significant discrepancies with the traditionally applied benthic oxygen isotope ($\delta^{18}\text{O}_b$) paleothermometer. In all instances, Δ_{47} -derived temperatures are higher than $\delta^{18}\text{O}_b$ -temperatures. There is a twofold of assumptions that may cause this: (1) the $\delta^{18}\text{O}$ of the seawater ($\delta^{18}\text{O}_w$) is assumed to be -0.98‰ , the value for an ice-free world, and (2) a potential pH effect in $\delta^{18}\text{O}_b$ is poorly understood and ignored. Moreover, Δ_{47} -temperatures do not correlate well with Mg/Ca-derived temperatures, most likely due to a multitude of assumptions in the latter proxy. In fact, Δ_{47} -temperatures allow the improvement of Mg/Ca by giving a way to calculate Mg/Ca ratios in the past oceans. Moreover, better constraints on the pH-effect of benthic foraminifera may allow much improvement of regular stable isotope data.

New values for $\delta^{18}\text{O}_w$ are calculated using the independent Δ_{47} -temperatures in the Marchitto et al. (2014) temperature calibration. The new $\delta^{18}\text{O}_w$ values display high discrepancies from the previously assumed value of -0.98‰ , even when a pH-correction is applied to $\delta^{18}\text{O}_b$. This matches well with other recent clumped isotope studies. The deviating $\delta^{18}\text{O}_w$, varying at Pleistocene-levels, has vast consequences for our understanding of the ‘ice-free’ Eocene. A variety of mechanisms are presented, including minor ice-sheets, aquifer-eustasy, hydrothermal input, and spatial salinity patterns. Neither are sufficient to explain all variance, and thus new hypotheses must be established.

A warming of $\sim 7.22 \pm 4.44\text{ °C}$ between 53 Ma and the maximum of the EECO in the deep ocean is not reflected by sea surface temperatures (SST), which raised a maximum of $\sim 4\text{ °C}$, but mostly leveled out in the same time span. This separation of the surface and deep ocean is in striking contrast with the classical view of the deep ocean, evolving in tandem with the surface. There are a variety of issues with TEX₈₆ when applied to past climates, particularly the temperature calibrations for the hothouse temperatures of the early Eocene, which could explain the stable SSTs. Still, this difference could bring new complications to estimates of the global surface temperature and polar amplification.

The heavy values for $\delta^{18}\text{O}_w$ along with high Δ_{47} -temperatures give rise to questions regarding ocean circulation. Given the uncertainties in temperature and seawater composition that comprise $\delta^{18}\text{O}_b$, it may well be that high salinity (and thus heavy $\delta^{18}\text{O}_w$) could have sourced from the warm, saline lower latitudes, rather than the cold, less saline Southern Ocean. This view has been debated previously but has recently been opposed by a general circulation model study that instead proposes the so-called ‘salt-advection feedback’. This mechanism involves that highly saline, heavy $\delta^{18}\text{O}_w$ -subtropical waters are advected to the subpolar gyres, where deep water is formed, while light $\delta^{18}\text{O}_w$ is rained out over the Northern Pacific. Tracing back deep waters, for example by extending Δ_{47} -records to the Southern Ocean and the Northern Pacific, could help with resolving this dichotomy.

Newly calculated values for global mean surface temperatures (GMST) and equilibrium climate sensitivity (ECS) fall in the higher ranges, specifically for the EECO with a climate sensitivity of $6.0\text{ °C}/2\times\text{CO}_2$, with a maximum of 9.1 and a minimum of $4.1\text{ °C}/2\times\text{CO}_2$. This means that previous estimates using $\delta^{18}\text{O}_b$ are most likely too low. The new estimates agree well with recent climate simulations that have enhanced cloud microphysics, and recent Mg/Ca and CO_2 evidence. The findings here support previous statements of climate state dependencies of ECS.

Acknowledgements

First and foremost, I want to thank my supervisors Tobias Agterhuis, Lucas Lourens, and Martin Ziegler for their great assistance, feedback, and guidance. I would also like to thank Natasja Welters and Giovanni Dammers for their assistance in the lab. In that respect, special thanks go to Desmond Eefting for his thorough help and patience with the Kiel IV and 253 Plus. I am also indebted to Ellen Thomas for her micropaleontological support. Further gratitude goes to Niels de Winter and Ilja Kocken for their discussions on- and help with the *R* programming language, as well as error propagation of the clumped temperature calibration.

Appendix: Foraminifera glossary

A list of definitions relevant to the micropaleontology of this study. Established with the help of Ellen Thomas and using the Atlas of Benthic Foraminifera by Holbourn, Henderson, and MacLeod (2013).

Biconvex: both sides look convex/spherical in side-view.

Bi-umbonate: umbilicus (umbo) on both sides.

Boss: centre platform in the umbilicus, also called *umbo*.

Evolute: almost all chambers/whorls are visible

Interiomarginal aperture: apertural slit borders the suture of the last chamber along the preceding coil (e.g. *Oridorsalis*).

Involute: only the last whorl is visible.

Lenticular: flattened convex, like lentils or a lens.

Lip: rim bordering the aperture.

Lobulate: inflated test or chambers, depressed sutures.

Periphery: the outer rim/edge of the foraminifera when looked at ventrally or dorsally.

Planispiral: the whirling of the tests occurs over one plane. Usually evolute on both sides (e.g. *Lenticulina*).

Planoconvex: one side is planar, the other convex.

Spiral side: evolute side (dorsal).

Tangential sutures: sutures have a straight appearance, rather than spiralling/curved.

Trochospiral: whirling over a horizontal plane but also in the vertical, like a spire. Usually evolute on one side, and involute on the other (e.g. *Cibicidoides*).

Umbilical side: the involute side for trochospiral foraminifera (ventral).

Umbilicus: inner space where chamber sutures join at the umbilical side.

References

- Agterhuis, T., M. Ziegler, N.J. De Winter, and L.J. Lourens. 2021. “Independent Constraints on Deep-Sea Temperatures across Two Early Eocene Hyperthermals from Clumped Isotope Thermometry.”
- Anagnostou, E., E.H. John, T.L. Babila, P.F. Sexton, A. Ridgwell, D.J. Lunt, P.N. Pearson, T.B. Chalk, R.D. Pancost, and G.L. Foster. 2020. “Proxy Evidence for State-Dependence of Climate Sensitivity in the Eocene Greenhouse.” *Nature Communications* 11 (1). <https://doi.org/10.1038/s41467-020-17887-x>.
- Anagnostou, E., E.H. John, K.M. Edgar, G.L. Foster, A. Ridgwell, G.N. Inglis, R.D. Pancost, D.J. Lunt, and P.N. Pearson. 2016. “Changing Atmospheric CO₂ Concentration Was the Primary Driver of Early Cenozoic Climate.” *Nature* 533 (7603): 380–84. <https://doi.org/10.1038/nature17423>.
- Batenburg, S.J., S. Voigt, O. Friedrich, A.H. Osborne, A. Bornemann, T. Klein, L. Pérez-Díaz, and M. Frank. 2018. “Major Intensification of Atlantic Overturning Circulation at the Onset of Paleogene Greenhouse Warmth.” *Nature Communications* 9 (1): 1–8. <https://doi.org/10.1038/s41467-018-07457-7>.
- Bernasconi, S.M., M. Daëron, K.D. Bergmann, M. Bonifacie, A.N. Meckler, H.P. Affek, N. Anderson, et al. 2021. “InterCarb: A Community Effort to Improve Interlaboratory Standardization of the Carbonate Clumped Isotope Thermometer Using Carbonate Standards.” *Geochemistry, Geophysics, Geosystems* 22 (5): 1–25. <https://doi.org/10.1029/2020gc009588>.
- Bernasconi, S.M., B. Hu, U. Wacker, J. Fiebig, S.F.M. Breitenbach, and T. Rutz. 2013. “Background Effects on Faraday Collectors in Gas-Source Mass Spectrometry and Implications for Clumped Isotope Measurements.” *Rapid Communications in Mass Spectrometry* 27 (December 2012): 603–12. <https://doi.org/10.1002/rcm.6490>.
- Bernasconi, S.M., I.A. Müller, K.D. Bergmann, S.F.M. Breitenbach, A. Fernandez, D.A. Hodell, M. Jaggi, A.N. Meckler, I. Millan, and M. Ziegler. 2018. “Reducing Uncertainties in Carbonate Clumped Isotope Analysis Through Consistent Carbonate-Based Standardization.” *Geochemistry, Geophysics, Geosystems* 19 (9): 2895–2914. <https://doi.org/10.1029/2017GC007385>.
- Bigeleisen, J. 1955. “Statistical Mechanics of Isotopic Systems with Small Quantum Corrections. I. General Considerations and the Rule of the Geometric Mean.” *The Journal of Chemical Physics* 23 (12): 2264–67.
- Bijl, P.K., J.A.P. Bendle, S.M. Bohaty, J. Pross, S. Schouten, L. Tauxe, C.E. Stickley, et al. 2013. “Eocene Cooling Linked to Early Flow across the Tasmanian Gateway.” *Proceedings of the National Academy of Sciences of the United States of America* 110 (24): 9645–50. <https://doi.org/10.1073/pnas.1220872110>.
- Bijl, P.K., S. Schouten, A. Sluijs, G.J. Reichart, J.C. Zachos, and H. Brinkhuis. 2009. “Early Palaeogene Temperature Evolution of the Southwest Pacific Ocean.” *Nature* 461 (7265): 776–79. <https://doi.org/10.1038/nature08399>.
- Bijma, J., H.J. Spero, and D.W. Lea. 1999. *Reassessing Foraminiferal Stable Isotope Geochemistry: Impact of the Oceanic Carbonate System (Experimental Results). Use of Proxies in Paleoceanography: Examples from the South Atlantic*. https://doi.org/10.1007/978-3-642-58646-0_20.
- Bornemann, A., R.D. Norris, O. Friedrich, B. Beckmann, S. Schouten, J.S. Sinninghe Damsté, J. Vogel, P. Hofmann, and T. Wagner. 2008. “Isotopic Evidence for Glaciation during the Cretaceous Supergreenhouse.” *Science* 319 (5860): 189–92. <https://doi.org/10.1126/science.1148777>.
- Bowen, G., B.J. Maibauer, M.J. Kraus, U. Röhl, T. Westerhold, A. Steimke, P.D. Gingerich, S.L. Wing, and W.C. Clyde. 2014. “Two Massive, Rapid Releases of Carbon during the Onset of the Palaeocene-Eocene Thermal Maximum.” *Nature Geoscience* 8 (1): 44–47. <https://doi.org/10.1038/ngeo2316>.
- Byrne, B., and C. Goldblatt. 2014. “Radiative Forcing at High Concentrations of Well-Mixed Greenhouse Gases.” *Geophysical Research Letters* 41 (1): 152–60. <https://doi.org/10.1002/2013GL058456>.

- Carmichael, M.J., G.N. Inglis, M.P.S. Badger, B.D.A. Naafs, L. Behrooz, S. Remmelzwaal, F.M. Monteiro, et al. 2017. "Hydrological and Associated Biogeochemical Consequences of Rapid Global Warming during the Paleocene-Eocene Thermal Maximum." *Global and Planetary Change* 157 (August): 114–38. <https://doi.org/10.1016/j.gloplacha.2017.07.014>.
- Carmichael, M.J., D.J. Lunt, M. Huber, M. Heinemann, J. Kiehl, A. LeGrande, C.A. Loptson, et al. 2016. "A Model-Model and Data-Model Comparison for the Early Eocene Hydrological Cycle." *Climate of the Past* 12 (2): 455–81. <https://doi.org/10.5194/cp-12-455-2016>.
- Coggon, R.M., D.A.H. Teagle, C.E. Smith-duque, J.C. Alt, and M.J. Cooper. 2010. "Reconstructing Past Seawater Mg/Ca and Sr/Ca from Mid-Ocean Ridge Flank Calcium Carbonate Veins." *Science* 327 (5969): 1114–17.
- Conrad, C..P., and C. Lithgow-Bertelloni. 2007. "Faster Seafloor Spreading and Lithosphere Production during the Mid-Cenozoic." *Geology* 35 (1): 29–32. <https://doi.org/10.1130/G22759A.1>.
- Conte, M.H., A. Thompson, G. Eglinton, and J.C. Green. 1995. "Lipid Biomarker Diversity in the Coccolithophorid *Emiliania Huxleyi* (Prymnesiophyceae) and the Related Species *Gephyrocapsa Oceanica*." *Journal of Phycology* 31 (2): 272–82. <https://doi.org/10.1111/j.0022-3646.1995.00272.x>.
- Cramer, B.S., K.G. Miller, P.J. Barrett, and J.D. Wright. 2011. "Late Cretaceous-Neogene Trends in Deep Ocean Temperature and Continental Ice Volume: Reconciling Records of Benthic Foraminiferal Geochemistry ($\Delta 18\text{O}$ and Mg/Ca) with Sea Level History." *Journal of Geophysical Research: Oceans* 116 (12): 1–23. <https://doi.org/10.1029/2011JC007255>.
- Cramwinckel, M.J., M. Huber, I.J. Kocken, C. Agnini, P.K. Bijl, S.M. Bohaty, J. Frieling, et al. 2018. "Synchronous Tropical and Polar Temperature Evolution in the Eocene." *Nature* 559 (7714): 382–86. <https://doi.org/10.1038/s41586-018-0272-2>.
- Davies, A., B. Gréselle, S.J. Hunter, G. Baines, C. Robson, A.M. Haywood, D.C. Ray, M.D. Simmons, and F.S.P. van Buchem. 2020. "Assessing the Impact of Aquifer-Eustasy on Short-Term Cretaceous Sea-Level." *Cretaceous Research* 112. <https://doi.org/10.1016/j.cretres.2020.104445>.
- Dennis, K.J., H.P. Affek, B.H. Passey, D.P. Schrag, and J.M. Eiler. 2011. "Defining an Absolute Reference Frame for 'clumped' Isotope Studies of CO_2 ." *Geochimica et Cosmochimica Acta* 75 (22): 7117–31. <https://doi.org/10.1016/j.gca.2011.09.025>.
- Dunkley Jones, T., Y.L. Eley, W. Thomson, S.E. Greene, I. Mandel, K. Edgar, and J.A. Bendle. 2020. "OPTiMAL: A New Machine Learning Approach for GDGT-Based Palaeothermometry." *Climate of the Past* 16 (6): 2599–2617. <https://doi.org/10.5194/cp-16-2599-2020>.
- Edgar, K.M., H. Pälike, and P.A. Wilson. 2013. "Testing the Impact of Diagenesis on the $\Delta 18\text{O}$ and $\Delta 13\text{C}$ of Benthic Foraminiferal Calcite from a Sediment Burial Depth Transect in the Equatorial Pacific." *Paleoceanography* 28 (3): 468–80. <https://doi.org/10.1002/palo.20045>.
- Eiler, J.M. 2007. "'Clumped-Isotope' Geochemistry-The Study of Naturally-Occurring, Multiply-Substituted Isotopologues." *Earth and Planetary Science Letters* 262 (3–4): 309–27. <https://doi.org/10.1016/j.epsl.2007.08.020>.
- Eiler, J.M., and E. Schauble. 2004. " $^{18}\text{O}^{13}\text{C}^{16}\text{O}$ in Earth's Atmosphere." *Geochimica et Cosmochimica Acta* 68 (23): 4767–77. <https://doi.org/10.1016/j.gca.2004.05.035>.
- Elderfield, H., J. Yu, P. Anand, T. Kiefer, and B. Nyland. 2006. "Calibrations for Benthic Foraminiferal Mg/Ca Paleothermometry and the Carbonate Ion Hypothesis." *Earth and Planetary Science Letters* 250 (3–4): 633–49. <https://doi.org/10.1016/j.epsl.2006.07.041>.
- Epstein, S., R. Buchsbaum, H. Lowenstam, and H.C. Urey. 1951. "Carbonate-Water Isotopic Temperature Scale." *Bulletin of the Geological Society of America* 62: 417–26.
- Evans, D. 2021. "Deep Heat: Proxies, Miocene Ice, and an End in Sight for Paleoclimate Paradoxes?" *Paleoceanography and Paleoclimatology* 36 (e2020PA004174). <https://doi.org/10.1029/2020PA004174>.
- Evans, D., and W. Müller. 2012. "Deep Time Foraminifera Mg/Ca Paleothermometry: Nonlinear Correction for Secular Change in Seawater Mg/Ca." *Paleoceanography* 27 (4): 1–11. <https://doi.org/10.1029/2012PA002315>.

- Evans, D., N. Sagoo, W. Renema, L.J. Cotton, W. Müller, J.A. Todd, P.K. Saraswati, et al. 2018. "Eocene Greenhouse Climate Revealed by Coupled Clumped Isotope-Mg/Ca Thermometry." *Proceedings of the National Academy of Sciences of the United States of America* 115 (6): 1174–79. <https://doi.org/10.1073/pnas.1714744115>.
- Evans, D., B.S. Wade, M. Henahan, J. Erez, and W. Müller. 2016. "Revisiting Carbonate Chemistry Controls on Planktic Foraminifera Mg / Ca: Implications for Sea Surface Temperature and Hydrology Shifts over the Paleocene-Eocene Thermal Maximum and Eocene-Oligocene Transition." *Climate of the Past* 12 (4): 819–35. <https://doi.org/10.5194/cp-12-819-2016>.
- Ferreira, D., P. Cessi, H.K. Coxall, A. De Boer, H.A. Dijkstra, S.S. Drijfhout, T. Eldevik, et al. 2018. "Atlantic-Pacific Asymmetry in Deep Water Formation." *Annual Review of Earth and Planetary Sciences* 46: 327–52. <https://doi.org/10.1146/annurev-earth-082517-010045>.
- Frieling, J., A.I. Iakovleva, G.J. Reichart, G.N. Aleksandrova, Z.N. Gnibidenko, S. Schouten, and A. Sluijs. 2014. "Paleocene-Eocene Warming and Biotic Response in the Epicontinental West Siberian Sea." *Geology* 42 (9): 767–70. <https://doi.org/10.1130/G35724.1>.
- Ghosh, P., J. Adkins, H. Affek, B. Balta, W. Guo, E.A. Schauble, D. Schrag, and J.M. Eiler. 2006. "¹³C-¹⁸O Bonds in Carbonate Minerals: A New Kind of Paleothermometer." *Geochimica et Cosmochimica Acta* 70 (6): 1439–56. <https://doi.org/10.1016/j.gca.2005.11.014>.
- Guo, W. 2020. "Kinetic Clumped Isotope Fractionation in the DIC-H₂O-CO₂ System: Patterns, Controls, and Implications." *Geochimica et Cosmochimica Acta* 268: 230–57. <https://doi.org/10.1016/j.gca.2019.07.055>.
- Hansen, J., M. Sato, G. Russell, and P. Kharecha. 2013. "Climate Sensitivity, Sea Level and Atmospheric Carbon Dioxide." *Philosophical Transactions of the Royal Society A: Mathematical, Physical and Engineering Sciences* 371 (2011). <https://doi.org/10.1098/rsta.2012.0294>.
- Hay, W.W., R.M. DeConto, C.N. Wold, K.M. Wilson, S. Voigt, M. Schulz, A.R. Wold, et al. 1999. "Alternative Global Cretaceous Paleogeography." In *Evolution of the Cretaceous Ocean-Climate System*, edited by E. Barrera and C. Johnson, 332:1–47. Geological Society of America. <https://doi.org/10.1130/0-8137-2332-9.1>.
- He, B., G.A. Olack, and A.S. Colman. 2012. "Pressure Baseline Correction and High-Precision CO₂ Clumped-Isotope ($\Delta 47$) Measurements in Bellows and Micro-Volume Modes." *Rapid Communications in Mass Spectrometry* 26 (24): 2837–53. <https://doi.org/10.1002/rcm.6436>.
- Holbourn, A.E., A.S. Henderson, and N. MacLeod. 2013. *Atlas of Benthic Foraminifera*. Oxford, UK: Wiley-Blackwell. <https://doi.org/10.1002/9781118452493>.
- Hollis, C.J., T. Dunkley Jones, E. Anagnostou, P.K. Bijl, M.J. Cramwinckel, Ying Cui, G.R. Dickens, et al. 2019. "The DeepMIP Contribution to PMIP4: Methodologies for Selection, Compilation and Analysis of Latest Paleocene and Early Eocene Climate Proxy Data, Incorporating Version 0.1 of the DeepMIP Database." *Geoscientific Model Development* 12 (7): 3149–3206. <https://doi.org/10.5194/gmd-12-3149-2019>.
- Hollis, C.J., K.W.R. Taylor, L. Handley, R.D. Pancost, M. Huber, J.B. Creech, B.R. Hines, et al. 2012. "Early Paleogene Temperature History of the Southwest Pacific Ocean: Reconciling Proxies and Models." *Earth and Planetary Science Letters* 349–350: 53–66. <https://doi.org/10.1016/j.epsl.2012.06.024>.
- Huber, M., and L.C. Sloan. 2001. "Heat Transport, Deep Waters, and Thermal Gradients: Coupled Simulation of an Eocene Greenhouse Climate." *Geophysical Research Letters* 28 (18): 3481–84. <https://doi.org/10.1029/2001GL012943>.
- Huguet, C., J.H. Kim, G.J. de Lange, J.S. Sinninghe Damsté, and S. Schouten. 2009. "Effects of Long Term Oxidic Degradation on the U37K', TEX86 and BIT Organic Proxies." *Organic Geochemistry* 40 (12): 1188–94. <https://doi.org/10.1016/j.orggeochem.2009.09.003>.
- Huntington, K.W., J.M. Eiler, H.P. Affek, W. Guo, M. Bonifacie, L.Y. Yeung, N. Thiagarajan, et al. 2009. "Methods and Limitations of 'clumped' CO₂ Isotope ($\Delta 47$) Analysis by Gas-Source Isotope Ratiomass Spectrometry." *Journal of Mass Spectrometry* 44 (9): 1318–29. <https://doi.org/10.1002/jms.1614>.

- Inglis, G.N., F. Bragg, N.J. Burls, M.J. Cramwinckel, D. Evans, G.L. Foster, M. Huber, et al. 2020. "Global Mean Surface Temperature and Climate Sensitivity of the Early Eocene Climatic Optimum (EECO), Paleocene-Eocene Thermal Maximum (PETM), and Latest Paleocene." *Climate of the Past* 16 (5): 1953–68. <https://doi.org/10.5194/cp-16-1953-2020>.
- IPCC. 2014. "Climate Change 2014: Synthesis Report." Edited by R.K. Pachauri and L.A. Meyer. *Fifth Assessment Report of the Intergovernmental Panel on Climate Change*. Vol. 9781107025. Geneva: IPCC. <https://doi.org/10.1017/CBO9781139177245.003>.
- John, C.M., and D. Bowen. 2016. "Community Software for Challenging Isotope Analysis: First Applications of 'Easotope' to Clumped Isotopes." *Rapid Communications in Mass Spectrometry* 30 (21): 2285–2300. <https://doi.org/10.1002/rcm.7720>.
- Jones, Morgan T., Lawrence M.E. Percival, Ella W. Stokke, Joost Frieling, Tamsin A. Mather, Lars Riber, Brian A. Schubert, et al. 2019. "Mercury Anomalies across the Palaeocene-Eocene Thermal Maximum." *Climate of the Past* 15 (1): 217–36. <https://doi.org/10.5194/cp-15-217-2019>.
- Katz, M.E., D.R. Katz, J.D. Wright, K.G. Miller, D.K. Pak, N.. Schackleton, and E. Thomas. 2003. "Early Cenozoic Benthic Foraminiferal Isotopes: Species Reliability and Interspecies Correction Factors." *Paleoceanography* 18 (2): 1–12. <https://doi.org/10.1029/2002pa000798>.
- Kele, S., S.F.M. Breitenbach, E. Capezzuoli, A.N. Meckler, M. Ziegler, I.M. Millan, T. Kluge, et al. 2015. "Temperature Dependence of Oxygen- and Clumped Isotope Fractionation in Carbonates: A Study of Travertines and Tufas in the 6–95°C Temperature Range." *Geochimica et Cosmochimica Acta* 168: 172–92. <https://doi.org/10.1016/j.gca.2015.06.032>.
- Kent, D. V., B. S. Cramer, L. Lanci, D. Wang, J. D. Wright, and R. Van der Voo. 2003. "A Case for a Comet Impact Trigger for the Paleocene/Eocene Thermal Maximum and Carbon Isotope Excursion." *Earth and Planetary Science Letters* 211 (1–2): 13–26. [https://doi.org/10.1016/S0012-821X\(03\)00188-2](https://doi.org/10.1016/S0012-821X(03)00188-2).
- Kim, S.T., A. Mucci, and B.E. Taylor. 2007. "Phosphoric Acid Fractionation Factors for Calcite and Aragonite between 25 and 75 °C: Revisited." *Chemical Geology* 246 (3–4): 135–46. <https://doi.org/10.1016/j.chemgeo.2007.08.005>.
- Kluge, T., C.M. John, R. Boch, and S. Kele. 2018. "Assessment of Factors Controlling Clumped Isotopes and $\Delta 18\text{O}$ Values of Hydrothermal Vent Calcites." *Geochemistry, Geophysics, Geosystems* 19 (6): 1844–58. <https://doi.org/10.1029/2017GC006969>.
- Kocken, I.J., I.A. Müller, and M. Ziegler. 2019. "Optimizing the Use of Carbonate Standards to Minimize Uncertainties in Clumped Isotope Data." *Geochemistry, Geophysics, Geosystems* 20 (11): 5565–77. <https://doi.org/10.1029/2019GC008545>.
- Lauretano, V., F.J. Hilgen, J.C. Zachos, and L.J. Lourens. 2016. "Astronomically Tuned Age Model for the Early Eocene Carbon Isotope Events: A New High-Resolution $\Delta 13\text{C}$ benthic Record of ODP Site 1263 between ~ 49 and ~ 54 Ma." *Newsletters on Stratigraphy* 49 (2): 383–400. <https://doi.org/10.1127/nos/2016/0077>.
- Lauretano, V., K. Littler, M. Polling, J.C. Zachos, and L.J. Lourens. 2015. "Frequency, Magnitude and Character of Hyperthermal Events at the Onset of the Early Eocene Climatic Optimum." *Climate of the Past* 11 (10): 1313–24. <https://doi.org/10.5194/cp-11-1313-2015>.
- Lauretano, V., J.C. Zachos, and L.J. Lourens. 2018. "Orbitally Paced Carbon and Deep-Sea Temperature Changes at the Peak of the Early Eocene Climatic Optimum." *Paleoceanography and Paleoclimatology* 33 (10): 1050–65. <https://doi.org/10.1029/2018PA003422>.
- Lear, C.H., H. Elderfield, and P.A. Wilson. 2000. "Cenozoic Deep-Sea Temperatures and Global Ice Volumes from Mg/Ca in Benthic Foraminiferal Calcite." *Science* 287 (5451): 269–72. <https://doi.org/10.1126/science.287.5451.269>.
- Lear, C.H., E.M. Mawbey, and Y. Rosenthal. 2010. "Cenozoic Benthic Foraminiferal Mg/Ca and Li/Ca Records: Toward Unlocking Temperatures and Saturation States." *Paleoceanography* 25 (4): 1–11. <https://doi.org/10.1029/2009PA001880>.
- Leutert, T.J., S. Modestou, S. Bernasconi, and A.N. Meckler. 2020. "Southern Ocean Bottom Water

- Cooling and Ice Sheet Expansion during the Middle Miocene Climate Transition.” *Climate of the Past Discussions*, no. December: 1–26. <https://doi.org/10.5194/cp-2020-157>.
- Leutert, T.J., P.F. Sexton, A. Tripathi, A. Piasecki, S.L. Ho, and A. Nele Meckler. 2019. “Sensitivity of Clumped Isotope Temperatures in Fossil Benthic and Planktic Foraminifera to Diagenetic Alteration.” *Geochimica et Cosmochimica Acta* 257: 354–72. <https://doi.org/10.1016/j.gca.2019.05.005>.
- Lisiecki, L.E., and M.E. Raymo. 2005. “A Pliocene-Pleistocene Stack of 57 Globally Distributed Benthic δ 18O Records.” *Paleoceanography* 20 (1): 1–17. <https://doi.org/10.1029/2004PA001071>.
- Lourens, L.J., A. Sluijs, D. Kroon, J.C. Zachos, E. Thomas, U. Röhl, J. Bowles, and I. Raffi. 2005. “Astronomical Pacing of Late Palaeocene to Early Eocene Global Warming Events.” *Nature* 435 (7045): 1083–87. <https://doi.org/10.1038/nature03814>.
- Lunt, D.J., F. Bragg, W.L. Chan, D.K. Hutchinson, J.B. Ladant, P. Morozova, I. Niezgodzki, et al. 2021. “DeepMIP: Model Intercomparison of Early Eocene Climatic Optimum (EECO) Large-Scale Climate Features and Comparison with Proxy Data.” *Climate of the Past* 17 (1): 203–27. <https://doi.org/10.5194/cp-17-203-2021>.
- Lunt, D.J., P.J. Valdes, T.D. Jones, A. Ridgwell, A.M. Haywood, D.N. Schmidt, R. Marsh, and M. Maslin. 2010. “CO₂-Driven Ocean Circulation Changes as an Amplifier of Paleocene-Eocene Thermal Maximum Hydrate Destabilization.” *Geology* 38 (10): 875–78. <https://doi.org/10.1130/G31184.1>.
- Lynch-Stieglitz, J., W.B. Curry, and N. Slowey. 1999. “A Geostrophic Transport Estimate for the Florida Current from the Oxygen Isotope Composition of Benthic Foraminifera.” *Paleoceanography* 14 (3): 360–73. <https://doi.org/10.1029/1999PA900001>.
- Marchitto, T.M., W.B. Curry, J. Lynch-Stieglitz, S.P. Bryan, K.M. Cobb, and D.C. Lund. 2014. “Improved Oxygen Isotope Temperature Calibrations for Cosmopolitan Benthic Foraminifera.” *Geochimica et Cosmochimica Acta* 130: 1–11. <https://doi.org/10.1016/j.gca.2013.12.034>.
- Meckler, A.N., P.F. Sexton, A.M. Piasecki, T.J. Leutert, J. Marquardt, M. Ziegler, T. Agterhuis, et al. 2021. “Cenozoic Evolution of Deep Ocean Temperature from Clumped Isotope Thermometry.”
- Meckler, A.N., M. Ziegler, M.I. Millán, S.F.M. Breitenbach, and S.M. Bernasconi. 2014. “Long-Term Performance of the Kiel Carbonate Device with a New Correction Scheme for Clumped Isotope Measurements.” *Rapid Communications in Mass Spectrometry* 28 (15): 1705–15. <https://doi.org/10.1002/rcm.6949>.
- Meinicke, N., S.L. Ho, B. Hannisdal, D. Nürnberg, A. Tripathi, R. Schiebel, and A.N. Meckler. 2020. “A Robust Calibration of the Clumped Isotopes to Temperature Relationship for Foraminifers.” *Geochimica et Cosmochimica Acta* 270: 160–83. <https://doi.org/10.1016/j.gca.2019.11.022>.
- Meinicke, N., M.A. Reimi, A.C. Ravelo, and A.N. Meckler. 2021. “Coupled Mg/Ca and Clumped Isotope Measurements Indicate Lack of Substantial Mixed Layer Cooling in the Western Pacific Warm Pool During the Last ~5 Million Years.” *Paleoceanography and Paleoclimatology* 36 (8): 1–25. <https://doi.org/10.1029/2020pa004115>.
- Miller, K.G., J.V. Browning, W. John Schmelz, R.E. Kopp, G.S. Mountain, and J.D. Wright. 2020. “Cenozoic Sea-Level and Cryospheric Evolution from Deep-Sea Geochemical and Continental Margin Records.” *Science Advances* 6 (20). <https://doi.org/10.1126/sciadv.aaz1346>.
- Miller, K.G., J.D. Wright, and J.V. Browning. 2005. “Visions of Ice Sheets in a Greenhouse World.” *Marine Geology* 217 (3–4): 215–31. <https://doi.org/10.1016/j.margeo.2005.02.007>.
- Modestou, S.E., T.J. Leutert, A. Fernandez, C.H. Lear, and A.N. Meckler. 2020. “Warm Middle Miocene Indian Ocean Bottom Water Temperatures: Comparison of Clumped Isotope and Mg/Ca-Based Estimates.” *Paleoceanography and Paleoclimatology* 35 (11). <https://doi.org/10.1029/2020PA003927>.
- Mollenhauer, G., M. Kienast, F. Lamy, H. Meggers, R.R. Schneider, J.M. Hayes, and T.I. Eglinton. 2005. “An Evaluation of ¹⁴C Age Relationships between Co-Occurring Foraminifera, Alkenones, and Total Organic Carbon in Continental Margin Sediments.” *Paleoceanography* 20 (1): 1–12. <https://doi.org/10.1029/2004PA001103>.

- Müller, I.A., A. Fernandez, J. Radke, J. van Dijk, D. Bowen, J. Schwieters, and S.M. Bernasconi. 2017. "Carbonate Clumped Isotope Analyses with the Long-Integration Dual-Inlet (LIDI) Workflow: Scratching at the Lower Sample Weight Boundaries." *Rapid Communications in Mass Spectrometry* 31 (12): 1057–66. <https://doi.org/10.1002/rcm.7878>.
- Müller, I.A., J.D. Rodriguez-Blanco, J.C. Storck, G.S. do Nascimento, T.R.R. Bontognali, C. Vasconcelos, L.G. Benning, and S.M. Bernasconi. 2019. "Calibration of the Oxygen and Clumped Isotope Thermometers for (Proto-)Dolomite Based on Synthetic and Natural Carbonates." *Chemical Geology* 525 (December 2018): 1–17. <https://doi.org/10.1016/j.chemgeo.2019.07.014>.
- Nunes, F., and R.D. Norris. 2006. "Abrupt Reversal in Ocean Overturning during the Palaeocene/Eocene Warm Period." *Nature* 439 (7072): 60–63. <https://doi.org/10.1038/nature04386>.
- Passey, B.H., N.E. Levin, T.E. Cerling, F.H. Brown, and J.M. Eiler. 2010. "High-Temperature Environments of Human Evolution in East Africa Based on Bond Ordering in Paleosol Carbonates." *Proceedings of the National Academy of Sciences of the United States of America* 107 (25): 11245–49. <https://doi.org/10.1073/pnas.1001824107>.
- Pearson, P.N., and M.R. Palmer. 2000. "Atmospheric Carbon Dioxide Concentrations over the Past 60 Million Years." *Nature* 406 (6797): 695–99. <https://doi.org/10.1038/35021000>.
- Rae, J.W.B. 2018. "Boron Isotopes in Foraminifera: Systematics, Biomineralisation, and CO₂ Reconstruction." In *Boron Isotopes: The Fifth Element*, edited by Horst Marschall and Gavin Foster, 107–43. Cham: Springer International Publishing. https://doi.org/10.1007/978-3-319-64666-4_5.
- Rae, J.W.B., Y-G. Zhang, X. Liu, G.L. Foster, and H.M. Stoll. 2021. "Atmospheric CO₂ over the Last 66 Million Years from Marine Archives." *Annual Review of Earth and Planetary Sciences*, 599–631.
- Rathmann, S., S. Hess, H. Kuhnert, and S. Mulitza. 2004. "Mg/Ca Ratios of the Benthic Foraminifera *Oridorsalis Umbonatus* Obtained by Laser Ablation from Core Top Sediments: Relationship to Bottom Water Temperature." *Geochemistry, Geophysics, Geosystems* 5 (12): 1–10. <https://doi.org/10.1029/2004GC000808>.
- Rathmann, S., and H. Kuhnert. 2008. "Carbonate Ion Effect on Mg/Ca, Sr/Ca and Stable Isotopes on the Benthic Foraminifera *Oridorsalis Umbonatus* off Namibia." *Marine Micropaleontology* 66 (2): 120–33. <https://doi.org/10.1016/j.marmicro.2007.08.001>.
- Ravelo, A.C., and C. Hillaire-Marcel. 2007. "The Use of Oxygen and Carbon Isotopes of Foraminifera in Paleooceanography." In *Developments in Marine Geology*, 1:735–64. Elsevier B.V. [https://doi.org/10.1016/S1572-5480\(07\)01023-8](https://doi.org/10.1016/S1572-5480(07)01023-8).
- Sames, B., M. Wagreich, C.P. Conrad, and S. Iqbal. 2020. "Aquifer-Eustasy as the Main Driver of Short-Term Sea-Level Fluctuations during Cretaceous Hothouse Climate Phases." *Geological Society Special Publication* 498 (1): 9–38. <https://doi.org/10.1144/SP498-2019-105>.
- Schrag, D.P., D.J. DePaolo, and F.M. Richter. 1995. "Reconstructing Past Sea Surface Temperatures: Correcting for Diagenesis of Bulk Marine Carbonate." *Geochimica et Cosmochimica Acta* 59 (11): 2265–78. [https://doi.org/10.1016/0016-7037\(95\)00105-9](https://doi.org/10.1016/0016-7037(95)00105-9).
- Shah, S.R., G. Mollenhauer, N. Ohkouchi, T.I. Eglinton, and A. Pearson. 2008. "Origins of Archaeal Tetraether Lipids in Sediments: Insights from Radiocarbon Analysis." *Geochimica et Cosmochimica Acta* 72 (18): 4577–94. <https://doi.org/10.1016/j.gca.2008.06.021>.
- Shipboard Scientific Party. 2004. "Proceedings of the Ocean Drilling Program, 208 Initial Reports." *Proceedings of the Ocean Drilling Program, 208 Initial Reports* 208. <https://doi.org/10.2973/odp.proc.ir.208.2004>.
- Sluijs, A., G J Bowen, H Brinkhuis, L J Lourens, and E Thomas. 2007. "The Palaeocene-Eocene Thermal Maximum Super Greenhouse: Biotic and Geochemical Signatures, Age Models and Mechanisms of Global Change." *Deep-Time Perspectives on Climate Change: Marrying the Signal from Computer Models and Biological Proxies* 1: 323–49. <https://doi.org/10.1017/9780521875000.015>.
- Spencer, C., and S.T. Kim. 2015. "Carbonate Clumped Isotope Paleothermometry: A Review of Recent Advances in CO₂ Gas Evolution, Purification, Measurement and Standardization Techniques."

- Geosciences Journal* 19 (2): 357–74. <https://doi.org/10.1007/s12303-015-0018-1>.
- Spero, H.J., J. Bijma, D.W. Lea, and B.E. Bernis. 1997. "Effect of Seawater Carbonate Concentration on Foraminiferal Carbon and Oxygen Isotopes." *Nature* 390 (6659): 497–500. <https://doi.org/10.1038/37333>.
- Tierney, J.E. 2013. *Biomarker-Based Inferences of Past Climate: The TEX86 Paleotemperature Proxy. Treatise on Geochemistry: Second Edition*. 2nd ed. Vol. 12. Elsevier Ltd. <https://doi.org/10.1016/B978-0-08-095975-7.01032-9>.
- Tierney, J.E., and M.P. Tingley. 2015. "A TEX86 Surface Sediment Database and Extended Bayesian Calibration." *Scientific Data* 2: 1–10. <https://doi.org/10.1038/sdata.2015.29>.
- Tripati, A.K., J. Backman, H. Elderfield, and P. Ferretti. 2005. "Eocene Bipolar Glaciation Associated with Global Carbon Cycle Changes." *Nature* 436 (7049): 341–46. <https://doi.org/10.1038/nature03874>.
- Tripati, A.K., R.A. Eagle, N. Thiagarajan, A.C. Gagnon, H. Bauch, P.R. Halloran, and J.M. Eiler. 2010. "13C-18O Isotope Signatures and 'clumped Isotope' Thermometry in Foraminifera and Coccoliths." *Geochimica et Cosmochimica Acta* 74 (20): 5697–5717. <https://doi.org/10.1016/j.gca.2010.07.006>.
- Tripati, A.K., and H. Elderfield. 2005. "Deep-Sea Temperature and Circulation Changes at the Paleocene-Eocene Thermal Maximum." *Science* 308 (5730): 1894–98. <https://doi.org/10.1126/science.1109202>.
- Tripati, A.K., P.S. Hill, R.A. Eagle, J.L. Mosenfelder, J. Tang, E.A. Schauble, J.M. Eiler, et al. 2015. "Beyond Temperature: Clumped Isotope Signatures in Dissolved Inorganic Carbon Species and the Influence of Solution Chemistry on Carbonate Mineral Composition." *Geochimica et Cosmochimica Acta* 166: 344–71. <https://doi.org/10.1016/j.gca.2015.06.021>.
- Uchikawa, J., and R.E. Zeebe. 2010. "Examining Possible Effects of Seawater PH Decline on Foraminiferal Stable Isotopes during the Paleocene-Eocene Thermal Maximum." *Paleoceanography* 25 (2): 1–14. <https://doi.org/10.1029/2009PA001864>.
- Urey, H.C. 1947. "The Thermodynamic Properties of Isotopic Substances." *Journal of the Chemical Society*, 562–81.
- Wallmann, K. 2001. "The Geological Water Cycle and the Evolution of Marine $\Delta O_{18}O$ Values." *Geochimica et Cosmochimica Acta* 65 (15): 2469–85. [https://doi.org/10.1016/S0016-7037\(01\)00603-2](https://doi.org/10.1016/S0016-7037(01)00603-2).
- Wang, Z., E.A. Schauble, and J.M. Eiler. 2004. "Equilibrium Thermodynamics of Multiply Substituted Isotopologues of Molecular Gases." *Geochimica et Cosmochimica Acta* 68 (23): 4779–97. <https://doi.org/10.1016/j.gca.2004.05.039>.
- Wendler, J.E., I. Wendler, C. Vogt, and J. Kuss. 2016. "Link between Cyclic Eustatic Sea-Level Change and Continental Weathering: Evidence for Aquifer-Eustasy in the Cretaceous." *Palaeogeography, Palaeoclimatology, Palaeoecology* 441: 430–37. <https://doi.org/10.1016/j.palaeo.2015.08.014>.
- Westerhold, T., and U. Röhl. 2009. "High Resolution Cyclostratigraphy of the Early Eocene - New Insights into the Origin of the Cenozoic Cooling Trend." *Climate of the Past* 5 (3): 309–27. <https://doi.org/10.5194/cp-5-309-2009>.
- Westerhold, T., U. Röhl, B. Donner, and J.C. Zachos. 2018. "Global Extent of Early Eocene Hyperthermal Events: A New Pacific Benthic Foraminiferal Isotope Record From Shatsky Rise (ODP Site 1209)." *Paleoceanography and Paleoclimatology* 33 (6): 626–42. <https://doi.org/10.1029/2017PA003306>.
- Westerhold, T., U. Röhl, T. Frederichs, C. Agnini, I. Raffi, J.C. Zachos, and R.H. Wilkens. 2017. "Astronomical Calibration of the Ypresian Timescale: Implications for Seafloor Spreading Rates and the Chaotic Behavior of the Solar System?" *Climate of the Past* 13 (9): 1129–52. <https://doi.org/10.5194/cp-13-1129-2017>.
- Zachos, J.C., G.R. Dickens, and R.E. Zeebe. 2008. "An Early Cenozoic Perspective on Greenhouse Warming and Carbon-Cycle Dynamics." *Nature* 451 (7176): 279–83. <https://doi.org/10.1038/nature06588>.

- Zachos, J.C., H. Pagani, L. Sloan, E. Thomas, and K. Billups. 2001. "Trends, Rhythms, and Aberrations in Global Climate 65 Ma to Present." *Science* 292 (5517): 686–93. <https://doi.org/10.1126/science.1059412>.
- Zachos, J.C., U. Röhl, S.A. Schellenberg, A. Sluijs, D.A. Hodell, D.C. Kelly, E. Thomas, et al. 2005. "Rapid Acidification of the Ocean during the Paleocene-Eocene Thermal Maximum." *Science* 308 (5728): 1611–15. <https://doi.org/10.1126/science.1109004>.
- Zachos, J.C., L.D. Stott, and K.C. Lohmann. 1994. "Evolution of Early Cenozoic Marine Temperatures." *Paleoceanography* 9 (2): 353–87. <https://doi.org/10.1029/93PA03266>.
- Zeebe, R.E. 1999. "An Explanation of the Effect of Seawater Carbonate Concentration on Foraminiferal Oxygen Isotopes." *Geochimica et Cosmochimica Acta* 63 (13–14): 2001–7. [https://doi.org/10.1016/S0016-7037\(99\)00091-5](https://doi.org/10.1016/S0016-7037(99)00091-5).
- . 2001. "Seawater PH and Isotopic Paleotemperatures of Cretaceous Oceans." *Palaeogeography, Palaeoclimatology, Palaeoecology* 170 (1–2): 49–57. [https://doi.org/10.1016/S0031-0182\(01\)00226-7](https://doi.org/10.1016/S0031-0182(01)00226-7).
- Zeebe, R.E., J. Bijma, B. Hönisch, A. Sanyal, H.J. Spero, and D.A. Wolf-gladrow. 2008. "Vital Effects and beyond: A Modelling Perspective on Developing Palaeoceanographical Proxy Relationships in Foraminifera." *Geological Society Special Publication* 303: 45–58. <https://doi.org/10.1144/SP303.4>.
- Zhang, Y., T. Huck, C. Lique, Y. Donnadieu, J.B. Ladant, M. Rabineau, and D. Aslanian. 2020. "Early Eocene Vigorous Ocean Overturning and Its Contribution to a Warm Southern Ocean." *Climate of The Past Discussions*, 1–35. <https://doi.org/10.5194/cp-2019-163>.
- Zhang, Y.G., M. Pagani, and Z. Wang. 2016. "Ring Index: A New Strategy to Evaluate the Integrity of TEX86 Paleothermometry." *Paleoceanography* 31 (2): 220–32. <https://doi.org/10.1002/2015PA002848>.
- Zhu, J., C.J. Poulsen, and J.E. Tierney. 2019. "Simulation of Eocene Extreme Warmth and High Climate Sensitivity through Cloud Feedbacks." *Science Advances* 5 (9): 1–11. <https://doi.org/10.1126/sciadv.aax1874>.